

NOTE TO USERS

This reproduction is the best copy available.

UMI[®]

A 2D Transverse Vortex Wind Tunnel for PIV Investigation of Airfoil Vortex Interaction

by

Daniel Brassard

B. Eng (Mechanical)

A thesis submitted to the Faculty of Graduate
Studies and Research in the partial fulfilment
of the requirements for the degree of

Master of Applied Science in Mechanical Engineering

(M.A.Sc.Mechanical)

Ottawa-Carleton Institute for Mechanical
and Aerospace Engineering

Department of Mechanical and Aerospace Engineering

Carleton University

Ottawa, Ontario

Canada

August, 2005

Copyright © 2005

Daniel Brassard



Library and
Archives Canada

Bibliothèque et
Archives Canada

Published Heritage
Branch

Direction du
Patrimoine de l'édition

395 Wellington Street
Ottawa ON K1A 0N4
Canada

395, rue Wellington
Ottawa ON K1A 0N4
Canada

Your file *Votre référence*
ISBN: 0-494-10082-6
Our file *Notre référence*
ISBN: 0-494-10082-6

NOTICE:

The author has granted a non-exclusive license allowing Library and Archives Canada to reproduce, publish, archive, preserve, conserve, communicate to the public by telecommunication or on the Internet, loan, distribute and sell theses worldwide, for commercial or non-commercial purposes, in microform, paper, electronic and/or any other formats.

The author retains copyright ownership and moral rights in this thesis. Neither the thesis nor substantial extracts from it may be printed or otherwise reproduced without the author's permission.

AVIS:

L'auteur a accordé une licence non exclusive permettant à la Bibliothèque et Archives Canada de reproduire, publier, archiver, sauvegarder, conserver, transmettre au public par télécommunication ou par l'Internet, prêter, distribuer et vendre des thèses partout dans le monde, à des fins commerciales ou autres, sur support microforme, papier, électronique et/ou autres formats.

L'auteur conserve la propriété du droit d'auteur et des droits moraux qui protègent cette thèse. Ni la thèse ni des extraits substantiels de celle-ci ne doivent être imprimés ou autrement reproduits sans son autorisation.

In compliance with the Canadian Privacy Act some supporting forms may have been removed from this thesis.

Conformément à la loi canadienne sur la protection de la vie privée, quelques formulaires secondaires ont été enlevés de cette thèse.

While these forms may be included in the document page count, their removal does not represent any loss of content from the thesis.

Bien que ces formulaires aient inclus dans la pagination, il n'y aura aucun contenu manquant.


Canada

The undersigned recommend to the Faculty of
Graduate Studies and Research acceptance of the thesis

**A 2D Transverse Vortex Wind Tunnel for PIV Investigation of Airfoil Vortex
Interaction**

submitted by

Daniel Brassard

B.Eng (Mechanical)

in partial fulfilment of the requirements for the degree
of Master of Applied Science in Mechanical Engineering

Thesis Co-Supervisor, Faculty Member: Dr. F. Nitzsche

Thesis Co-Supervisor, Faculty Member: Dr. D. Feszty

Chair, Department of Mechanical and Aerospace Engineering:

Dr. J.C. Beddoes

Carleton University

August 2005

For Mom and Dad

Abstract

A novel wind tunnel has been designed and built to allow PIV (Particle Image Velocimetry) investigation of 2D Airfoil Vortex Interaction (AVI). AVI is a simplified representation of parallel Blade Vortex Interaction (BVI), a phenomenon typical of rotorcraft aerodynamics and characterized by the interaction of the rotor wake vortex with subsequent blades. In AVI, the wake vortex is represented by a vortex, having a rotation axis perpendicular to the direction of the flow, convecting downstream and interacting with the target airfoil, representing the blade. The features of the wind tunnel include a high aspect ratio test section simulating 2D unbounded flow at 80 m/s, a novel design application of CFD for contraction optimization, the incorporation of a modestly priced commercial air-handling centrifugal blower as the wind tunnel fan, and the tunnel's compatibility with a proposed vortex generator, which permits the generation of a single, repeatable transverse vortex. The concept of this vortex generator is novel and involves plunging of an airfoil from the far field to the location of interest in the flow. When the airfoil motion is suddenly arrested, the bound vorticity accumulated due to the change in flow incidence caused by the plunge will "roll up" into a single vortex of predictable circulation and core diameter.

Acknowledgements

I would like to thank my thesis co-supervisors, Doctor Fred Nitzsche and Doctor Daniel Feszty. Also, I would like to thank Professor Peter Bradshaw of Stanford University for his help and guidance over the course of this and previous projects. Professor Bradshaw is probably the world's foremost authority on wind tunnel design. Mistakes belong to the author, successes are due to Professor Bradshaw.

It is especially important to thank the members of Mechanical Engineering Laboratory and machine shop at Carleton University, Fred Barrett, Stephan Biljan, Gary Clements, Alex Proctor, Jim Sliwka, and Steve Truttman.

Importantly, without the huge amount of assistance from Gregory Davis, it is no exaggeration to say that this project would not have been completed. Thanks, Davis.

Table of Contents

Abstract	iv
Acknowledgements	v
Table of Contents	vi
List of Figures	vii
List of Tables	ix
1. INTRODUCTION	- 1 -
1.1 Blade-Vortex Interaction (BVI).....	- 1 -
1.2 Overview of BVI/AVI Investigations.....	- 4 -
1.3 Vortex Generators in AVI studies.....	- 8 -
1.4 Objectives	- 10 -
2. DESIGN OF EXPERIMENT	- 11 -
2.1 The Vortex Generator	- 11 -
2.2 The Test Chamber.....	- 17 -
2.2.2 Viscous Wall Effects.....	- 21 -
2.2.3 Viscous Vortex Behaviour.....	- 22 -
2.3 Evaluation of Similarity Parameters	- 26 -
2.4 Design Modification	- 27 -
2.5 Instrumentation	- 28 -
3. WIND TUNNEL DESIGN REVIEW	- 29 -
3.1 The Wide Angle Diffuser (WAD)	- 30 -
3.2 The Settling Chamber	- 33 -
3.3 The Screens.....	- 33 -
3.4 The Contraction	- 36 -
3.5 The Test Chamber.....	- 38 -
3.6 Diffusers.....	- 39 -
3.7 Corners and Turning Vanes	- 40 -
3.8 The Fan or Blower	- 41 -
4. IMPLEMENTATION AND TESTING	- 43 -
4.1 Design Space.....	- 43 -
4.2 Lab Airflow Impact Study	- 45 -
4.3 Wide Angle Diffuser (WAD).....	- 48 -
4.4 The Settling Chamber	- 50 -
4.5 Screens	- 52 -
4.6 Testing outlet flow from Settling Chamber	- 53 -
4.7 Contraction.....	- 54 -
4.8 Test Chamber	- 58 -
4.9 Diffusers.....	- 60 -
4.10 Corner Vanes	- 62 -
4.11 The Blower.....	- 64 -
4.12 Test Chamber Flow Testing.....	- 67 -
5. CONCLUSIONS AND RECOMMENDATIONS	- 74 -

List of Figures

Figure 1: The principal BVIs, shown schematically. Those numbered 1, 2, 3 & 4, are the primary source of BVI noise, from Lee and Bershader, 1994.	2 -
Figure 2: 2D CFD simulation of a two dimensional airfoil-vortex interaction, according to Lee & Bershader, (1994). Note the sound wave generated by the airfoil-vortex interaction.	3 -
Figure 3: A plot generated through CFD of $C_{p,l}$ (Co-efficient of pressure on the lower surface) vs. time step for an AVI (Morvant, 2004).....	4 -
Figure 4: Typical arrangement of an aeroacoustic wind tunnel facility. Dimensions in meters.	6 -
Figure 5 : A longitudinal vortex generator and rotor BVI test setup.	7 -
Figure 6: Shock tube transonic wind tunnel vortex generating method, due to Mamou et al (2001).	8 -
Figure 7: Stream plots of a Von Karman street vortex, due to Lyn et al (1995)	9 -
Figure 8: A schematic representation of the proposed vortex generator system.	12 -
Figure 9: A plunging airfoil, shown with moving sidewalls. Note that the plunged airfoil is shown displaced downstream for clarity only,.....	13 -
Figure 10: A partially cutaway top view of the proposed vortex generator mechanism.-	14 -
Figure 11: The proposed one degree of freedom mass/spring plunging airfoil vortex generator.	14 -
Figure 12: Free Body Diagram of the proposed 1DOF system.	15 -
Figure 13: The velocity as a function of time of the 1DOF system represented by the proposed vortex generator.....	17 -
Figure 14: Schematic view of the proposed test section.....	18 -
Figure 15: An unconstrained, inviscid vortex of circulation $3.22 \text{ m}^2/\text{s}$	20 -
Figure 16: A constrained, inviscid vortex of circulation $3.22 \text{ m}^2/\text{s}$ constrained by walls at $\pm 0.3175 \text{ m}$	20 -
Figure 17: Viscous (solid) and Inviscid (dashed) values of circulation and tangential velocity expressed in terms of normalized radius $(r/(2vt))^{1/2}$	25 -
Figure 18: A schematic of a typical closed circuit wind tunnel.....	30 -
Figure 19: Overall Pressure drop coefficient (K_{sum}), the sum of all the pressure drop coefficients for the screens installed in the WAD, vs. area ratio (A) of the WAD for a diffuser with screens (Mehta & Bradshaw, 1979).	31 -
Figure 20: Design Boundaries for diffusers with screens (Mehta & Bradshaw, 1979) .-	32 -
Figure 21: Flow in the region of a screen, placed in the flow at an angle.	34 -
Figure 22: The effect of varying $f(\zeta)$, according to Eq. 3.5.....	38 -
Figure 23: Otherwise identical closed circuit tunnels, one employing an axial fan (left) the other employing a centrifugal blower (right). Note that one set of corner vanes is saved in the blower configuration.	42 -
Figure 24: The space available. All dimensions are in inches.	43 -

Figure 25: Schematic of the new tunnel concept, side and top views. A fifth corner turns the flow directly into the inlet of the blower.....	44 -
Figure 26: The tunnel placed in the available space.	44 -
Figure 27: Velocity profile associated with an unobstructed room, shown rotated for clarity.	47 -
Figure 28: Velocity profile associated with an obstructed room, shown rotated for clarity -	47 -
Figure 29: Schematic side view of the diffuser. Curved lines are locations for screens. Crossed circles are the center points for the screen locations depicted (Dimensions are inches).	48 -
Figure 30: The Wide Angle Diffuser, as implemented.....	50 -
Figure 31: Side view detail of screen mounting method in settling chamber.....	51 -
Figure 32: Detail of the Settling Chamber, as implemented.....	52 -
Figure 33: Mesh topology used in the CFD optimization of the contraction.	56 -
Figure 34: Normalized velocity contours for two contraction wall profiles, $f(\zeta)=0.5$ (a), and $f(\zeta)=0.137$ (b). Note the separation in the second case.....	57 -
Figure 35: The contraction, as implemented.....	58 -
Figure 36: Cross section view of the 2D test section. Easily constructed from aluminum structural shapes, the fastening of the walls to the floor and ceiling is by clamping pressure.	59 -
Figure 37: The test chamber, as implemented. Notice the slot milled in the bottom wall to permit the PIV laser to pass.	60 -
Figure 38: The present curved diffuser, shown hatched, between the test chamber (left) and the first corner (right).....	61 -
Figure 39: The diffuser immediately following the test chamber , as implemented. ...	62 -
Figure 40: Schematic view of the corner vane slots inscribed in medium density fiberboard, to create the first two corners.	63 -
Figure 41: The first and second corner vanes in their assembly, as implemented.....	64 -
Figure 42: Performance curves for selected centrifugal blower.	66 -
Figure 43: Performance curves for an axial fan, New York Blower model Vaneaxial 32”.-	66 -
Figure 44: Grid of velocities recorded at inlet and outlet of test chamber.	68 -
Figure 45: Velocity profiles in test chamber, associated with data from Table 7.	70 -
Figure 46: Detail of a rake manometer, connected to various points along the return path, as detailed in Figure 47.	71 -
Figure 47: The connection points of the rake manometer.	71 -
Figure 48: Airline diagram of the wind tunnel, all dimensions are in inches.	73 -

List of Tables

Table 1: Velocity measurements associated with an unobstructed room, positions are as seen from within the tunnel, looking upstream:.....	- 46 -
Table 2: Velocity measurements associated with an unobstructed room, positions are as seen from within the tunnel, looking upstream:.....	- 46 -
Table 3: Velocity readings at outlet of settling chamber, in m/s, trial 1.....	- 53 -
Table 4: Velocity readings at outlet of settling chamber, in m/s, trial 2.....	- 53 -
Table 5: Velocity readings at outlet of settling chamber, in m/s, trial 3.....	- 54 -
Table 6: Summary of head losses in the current wind tunnel.	- 65 -
Table 7: Test Chamber velocities.	- 69 -

1. INTRODUCTION

1.1 Blade-Vortex Interaction (BVI)

Rotorcraft are unique in that they can take off and land vertically, carry usefully large payloads, and travel at a reasonable speed and altitude in an economical fashion. This makes them ideal for a variety of military transport and tactical roles and civilian transport roles. Although helicopters in general have achieved a considerable maturity of technology there are still some areas which have not been adequately solved, especially those of vibration and noise. Excessive vibration limits forward flight velocity and increases maintenance costs due to fatigue of mechanical parts, while excessive noise limits the tactical flexibility of military aircraft and creates conflict between the helicopter's economic role in civilian aviation and its adherence to urban noise ordinances. In addition, both phenomena have a deleterious effect on passenger comfort, and prohibit a "jet smooth" ride.

Vibration and noise are both generated as a result of the complex aerodynamics associated with rotary-wing flight. One of the most significant phenomena responsible for them is Blade Vortex Interaction (BVI).

BVI occurs primarily in low speed descending flight. Normally, as in steady, level flight, the tip vortices of the blades are convected downwards, away from the rotor disk. The initiation of descent or flare can allow the path of the tip vortices and the rotor disk to intersect. When this happens, it can lead to an undesirable noise source (Lee &

Bershader, 1994). As shown in Figure 1, there are many different characteristic BVIs. In the case of main rotor tip vortices, where the axis of the vortex is roughly parallel to the leading edge of the blade, the phenomenon is termed parallel BVI.

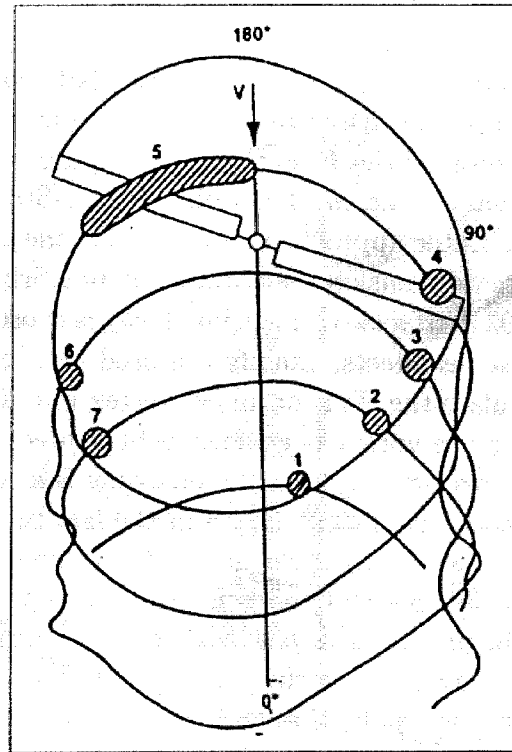


Figure 1: The principal BVIs, shown schematically. Those numbered 1, 2, 3 & 4, are the primary source of BVI noise, from Lee and Bershader, 1994.

In parallel BVI, the induced velocity provided by the vortex causes an extremely short duration change in the effective angle of attack of the blade. In some cases it can lead to a shockwave being released from the leading edge of the blade, whose propagation creates a characteristic and impulsive noise (Yu, 2000). It is supposed that a mechanism of this sound generation is the rapid movement of the stagnation point across the leading edge as the vortex passes causing the release of the sound wave due to

transonic effects (Korber & Ballman, 1995), although this is yet to be confirmed, given the extreme difficulties of analyzing such phenomenon. Work such as that of Lee and Bershader (1994), in which 2-D CFD simulations were performed (Figure 2), tends to support this conception. It is, however, proposed in this work that 2D investigation of BVI is more correctly termed Airfoil Vortex Interaction (AVI), since a “blade” must necessarily be a 3D object.

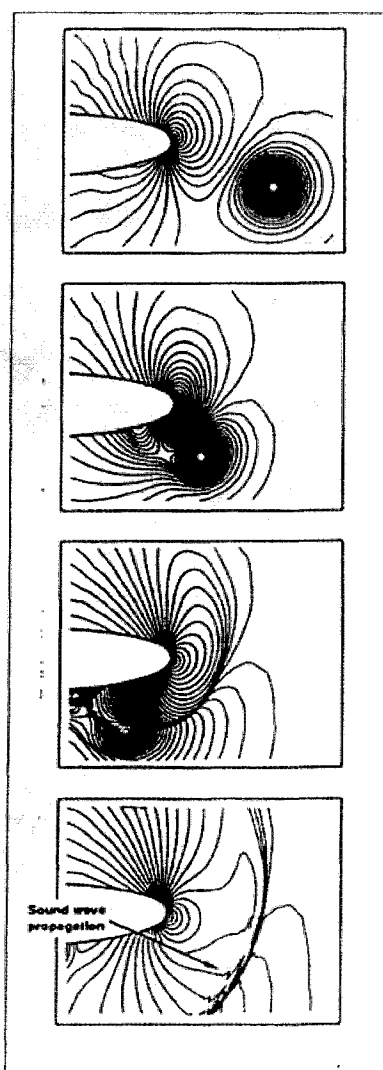


Figure 2: 2D CFD simulation of a two dimensional airfoil-vortex interaction, according to Lee & Bershader, (1994). Note the sound wave generated by the airfoil-vortex interaction.

BVI noise levels are typically in the 160 dB range, and radiate highly efficiently, as they are associated with shockwave release (Yu, 2000). Recent research has demonstrated that BVI also contributes to vibration by producing sudden variation in blade lift (Morvant, 2004), as shown in Figure 3. Therefore, reducing the effect of BVI is imperative to reduce overall vibration and noise, and so has received considerable interest as a research topic lately.

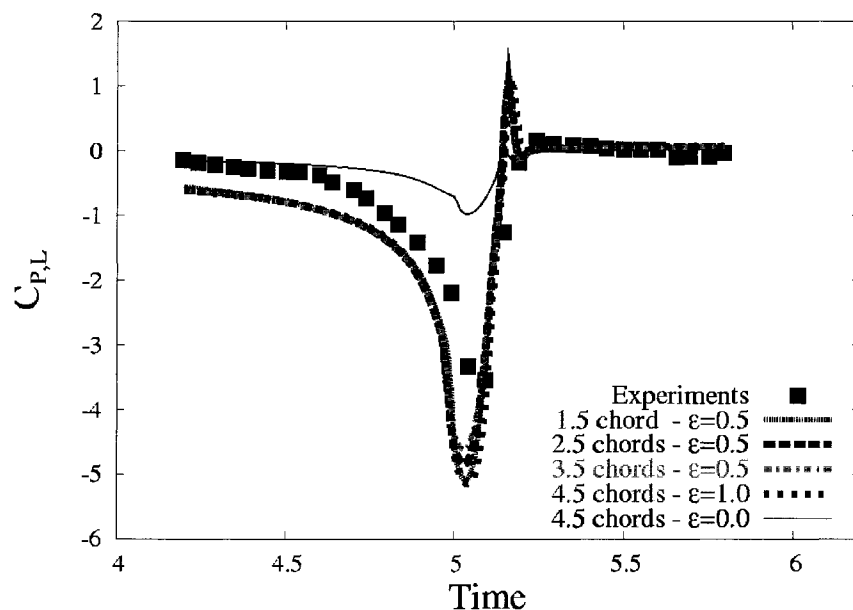


Figure 3: A plot generated through CFD of $C_{p,l}$ (Co-efficient of pressure on the lower surface) vs. time step for an AVI (Morvant, 2004)

1.2 Overview of BVI/AVI Investigations

As an aerodynamic phenomenon, BVI/AVI can be studied using CFD, but presents a variety of problems. Vortices represent numerical difficulties, as the region encompassing the highest gradients moves, so any grid optimized for one time step is far from optimal for the next. Morvant (2004) has shown good results using a vorticity

confinement method, in which a factor is chosen at which vorticity is re-introduced to the simulations to make up for that lost due to numerical dissipation. Although this approach works, it necessitates the fine tuning of the so called “confinement parameters” for every different case investigated, implying lengthy numerical experimentation. Studies have demonstrated that these BVI calculations take an extreme amount of computing power (Morvant, 2000). It is important to note that these delays and difficulties are related to study of 2D AVI. The study of a full 3-D BVI would be even more difficult.

Hence, the most common and reliable apparatus for the study of BVI and AVI remains the wind tunnel. Broadly speaking, previous experiments have involved three categories of experimental setups. The first is a model scale aeroacoustic setup (Figure 4), where a scale model of a rotor assembly is placed in a flow, and various flight regimes are simulated, until BVI noise occurs. The primary form of instrumentation for aeroacoustic tests are microphones placed around the rotor to gauge the intensity of the BVI noise. While this type of test is the best approximation of an in flight BVI, it is the most difficult to instrument, and by far the most expensive, in terms of a facility. Also, should one wish to use a flow visualization system, such as Particle Imaging Velocimetry, it can be very hard to assure proper particle densities in the areas where BVI noise originate. A good example of such an experimental setup is the HELINOISE program conducted at the DNW wind tunnel in the Netherlands (Splettstoesser *et al*, 1993).

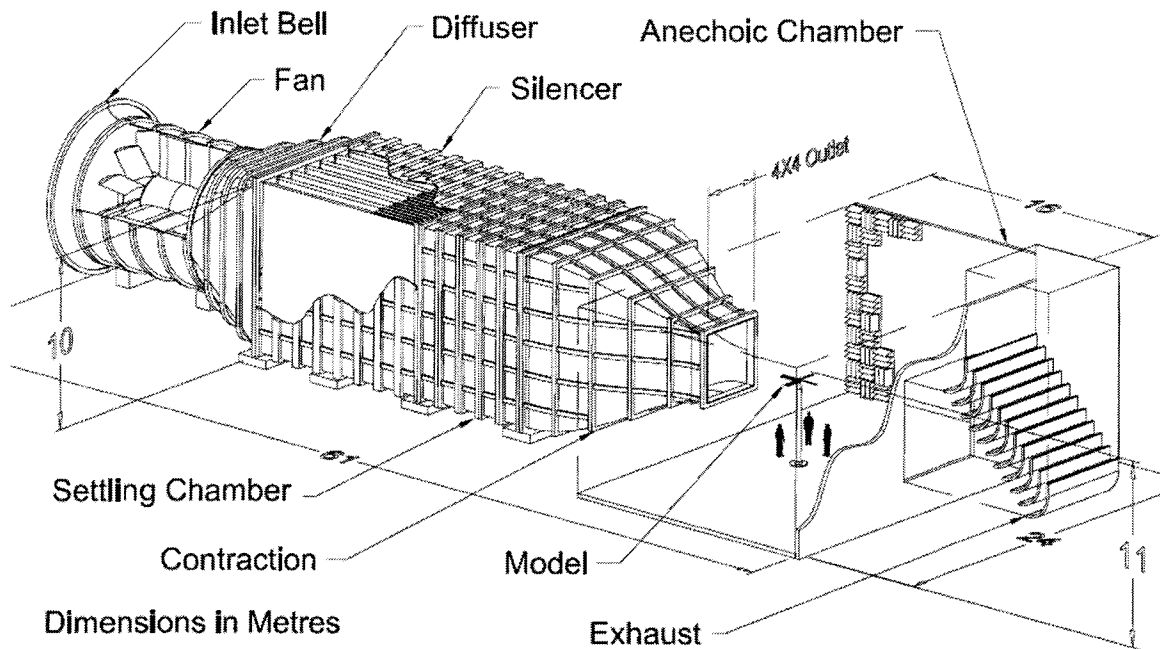


Figure 4: Typical arrangement of an aeroacoustic wind tunnel facility. Dimensions in meters.

Similar is the second arrangement, in which a fixed, finite airfoil, cantilevered at a constant angle of attack to the free stream, upstream of a rotor generates a vortex having an axis aligned with the direction of flow (Figure 5). As the rotor turns, the blade or blades interact with the vortex in a way that is similar to a rotorcraft BVI. The largest difference is the inclusion of a spanwise component of velocity much greater than what may be present in a true BVI. While the tunnel required for this sort of study is much more modest than an aeroacoustic facility, it is still considerable. Instrumenting the blade(s), for example with pressure taps, is as difficult as in the aeroacoustic facility. A convenience is that the region in which the BVI event occurs is known, and therefore it is straightforward to accomplish flow visualization and/or particle seeding in that area. This is the type of experimental setup used by Caradonna *et al*, (1988).

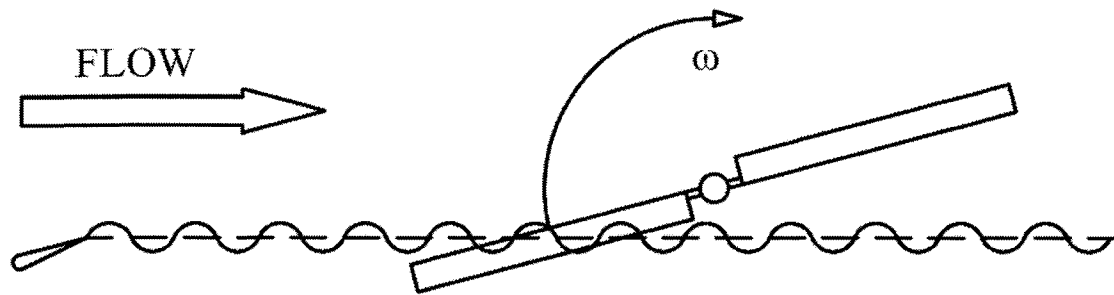


Figure 5 : A longitudinal vortex generator and rotor BVI test setup.

The third setup is entirely different from the other two in that it models an AVI in the wind tunnel, rather than a BVI. Typically, the target airfoil, representing the rotor blade, is fixed across the entire width of the tunnel. Some device upstream creates vortices, transverse to the direction of flow, which convect downstream and interact with the target airfoil. The interaction is two dimensional in that the airfoil and vortex are both bounded by the walls of the wind tunnel, implying an effectively infinite span. Strauss *et al* (1988) have validated this method of inquiry in low speed wind tunnels as being a useful representation of the rotorcraft BVI. Unfortunately, low speed tunnel studies (~ 30 m/s), required to render the conceived vortex generator mechanically simple, are flawed as neither dynamic nor Mach number similarity can be approached, let alone reached. Thus, while the interaction of the airfoil and vortex is measurable, it will not generate compressibility related noise.

1.3 Vortex Generators in AVI studies

AVI studies have been performed in transonic wind tunnels in two ways. First, using a shock tube to create a single vortex (Selerowicz *et al*, 1998), and second using a bluff body to create a Von Karman street upstream of the target airfoil (Lent *et al*, 1993). The vortex generating mechanism in the shock tube experiment is described by Mamou *et al* (2001), and involves the interaction of a shock wave moving downstream, and a fixed airfoil placed at an angle (Figure 6).

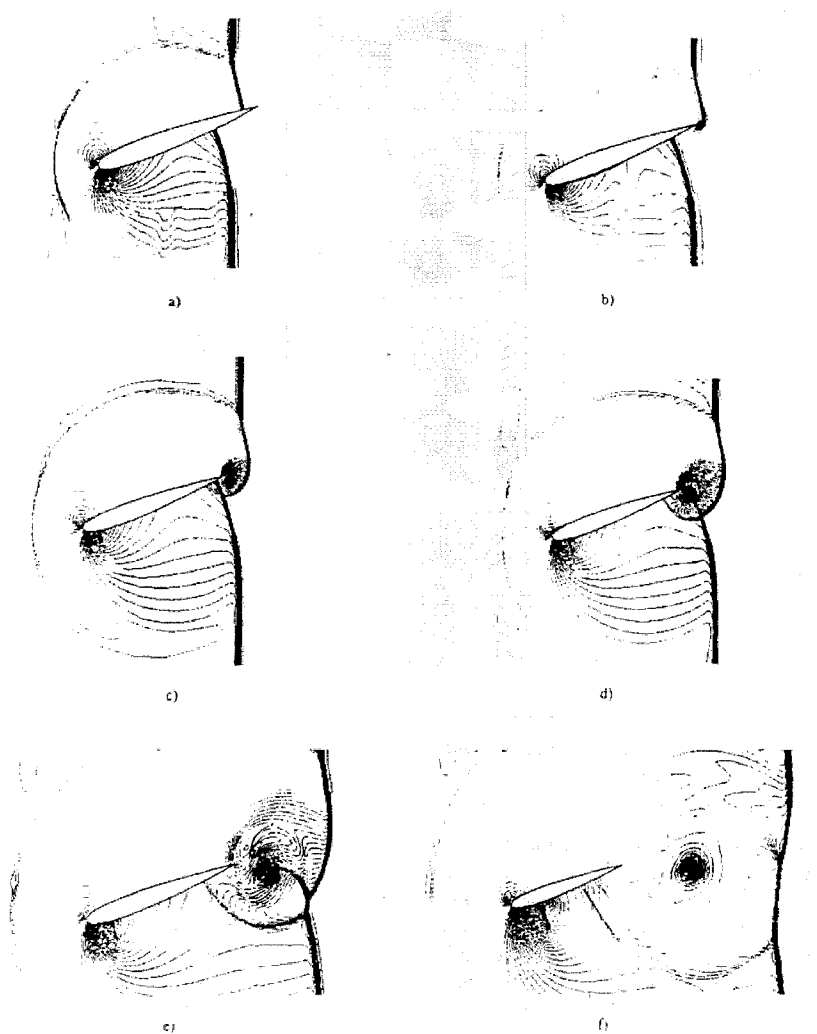


Figure 6: Shock tube transonic wind tunnel vortex generating method, due to Mamou et al (2001).

The second method, use of a bluff body to create a vortex street (Figure 7), suffers from the same weakness in the case of both low speed and transonic wind tunnels. Moreover, the vortices are in close proximity, so the results obtained from any single AVI can be expected to be contaminated by the proximity of the other vortices. Further, the circulation and shape of each vortex is not repeatedly identical, and is hardly predictable on a consistent basis.

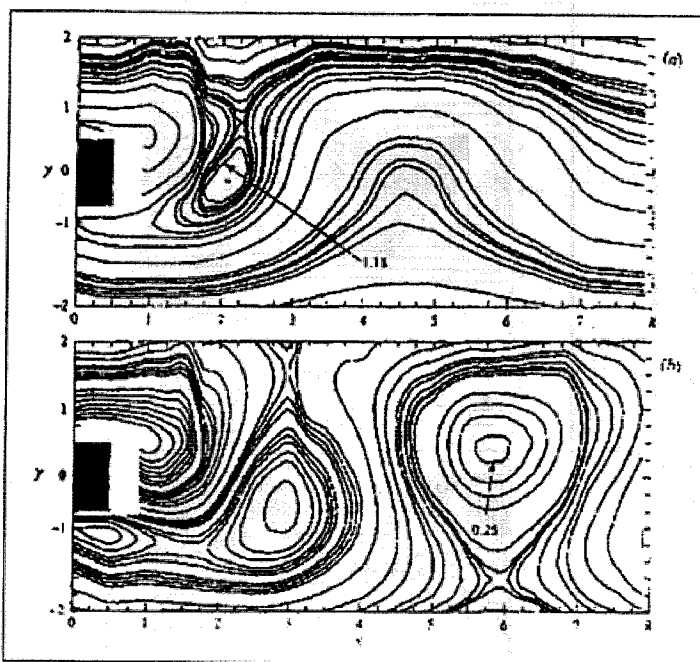


Figure 7: Stream plots of a Von Karman street vortex, due to Lyn et al (1995)

In order to space vortices a useful distance apart, and assure the rough equivalence of circulation between vortices, it has become common to use an oscillating airfoil to create the vortex street (Strauss *et al*, 1988). The sudden changes in the airfoil's angle of attack with the free stream create the familiar phenomenon of a starting vortex at the extremes of the airfoil angle. Strauss *et al* (1988) make the point that the change in angle, or relatively steady value of lift, must be accomplished in the time it takes flow to

pass one chord length. This system corrects some of the flaws associated with the use of the bluff body vortex generator, but leaves the probability of interference by subsequent vortices.

It is clear that all of the above (and common) approaches of generating a vortex for AVI experiments are non-ideal either due to the close proximity of vortices of opposite circulation, or the enormous cost and laboratory space necessary. It has been identified that ideally some mechanism should generate a single transverse (at right angles to the direction of flow) vortex which would convect downstream to interact with a target airfoil in the tunnel test section, where data would be collected (Wilder et al 1990).

1.4 Objectives

The objective of the present work is to design and implement the wind tunnel component of a cost effective experimental facility for the system characterization of BVI. This work includes the conceptual design of a vortex generator capable of generating one single vortex of predictable strength and convection path, transverse to the test chamber, around which the wind tunnel is designed. The facility should also allow flow visualization via Particle Imaging Velocimetry. The current work will consist of the implementation of the wind tunnel suitable to the experiment described here. Due to time constraints, this work will not include construction of the vortex generator, or installation of the PIV system.

2. DESIGN OF EXPERIMENT

For reasons of cost, and space limitation, it was decided to construct apparatus to conduct 2D AVI studies. The specific space constraints will be detailed in chapter 5. It was chosen to attempt to design a wind tunnel capable of 100 m/s or 0.3 Mach. This is considered as the threshold below which compressibility is inconsequential to design. The size should be on such a scale as to be able to test full chord length helicopter blade sections (30-60 cm). AVI wind tunnel studies require the generation of transverse vortices upstream of the target airfoil, so this is the first logical step.

2.1 The Vortex Generator

It has been shown in the previous chapter that a vortex generator for 2D AVI tests should ideally create just one single vortex to avoid contamination of experimental results from the street of vortices generated by bluff bodies or oscillating airfoils. No such vortex generator has been created to date and one objective of this thesis was to design such a novel experimental device.

The proposed vortex generator involves an airfoil plunged a much larger distance than customary and then braked rapidly in the desired area of the flow (Figure 8). The airfoil remains horizontal, but gathers its angle of attack, and therefore circulation, from the plunging action. Since the distance available for acceleration is larger, less force is required to reach a desired level of circulation. Also, stopping something rapidly is mechanically much easier than accelerating, analogous to an automobile, in which a

large, complex, and expensive motor is required to accelerate at a certain rate, but comparatively simple and inexpensive brakes are all that is required to decelerate at a similar rate.

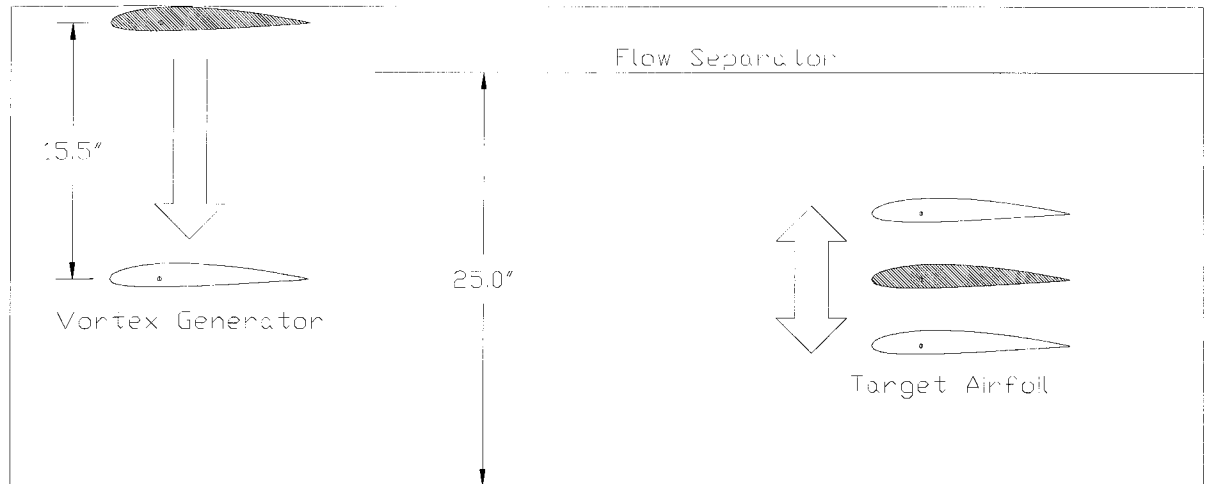


Figure 8: A schematic representation of the proposed vortex generator system.

The principle of operation of the conceived vortex generator involves the well-known phenomenon of a starting vortex. As the lift about an airfoil changes for any reason, be it a change in velocity, angle of attack, or camber shape, the circulation changes according to Kutta-Joukowski law:

$$L = \rho U_{\infty} \Gamma \quad (2.1)$$

Where L is the lift per unit span, ρ is the air density, U_{∞} is the free stream velocity, and Γ is the circulation about the body.

Vorticity is known to be a conservative property, so in order for the bound vorticity (circulation) around a body to change, vorticity must be continuously shed in an

equal-and-opposite fashion. Simple vortex dynamics hold that, should this change in bound vorticity happen rapidly enough, it will “roll up” into a single, coherent vortex (Strauss *et al*, 1998).

Since the far field inside a wind tunnel test section cannot extend beyond its walls, a slight raising of the top wall is proposed to allow for the inclusion of a flow separator 10 cm from the top wall in the hope that it separates the worst of any unsteady wake from the interrogation area.

Moving an airfoil in this fashion in a 2D test section requires the plunged airfoil be attached to two sections of moving sidewall, as shown in Figure 9. Since the walls cannot be aligned to be perfectly flush, it is deemed desirable to present a small but positive forward facing step to the flow. It is understood that a forward facing step affords a greater opportunity for boundary layer separation to re-attach, as compared to a rearward facing step. This is shown in Figure 10.

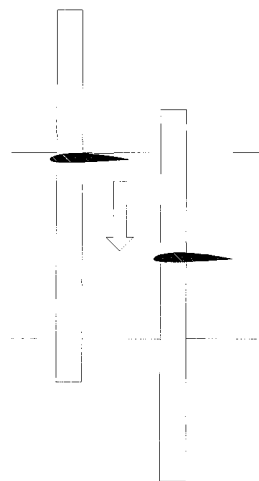


Figure 9: A plunging airfoil, shown with moving sidewalls. Note that the plunged airfoil is shown displaced downstream for clarity only,

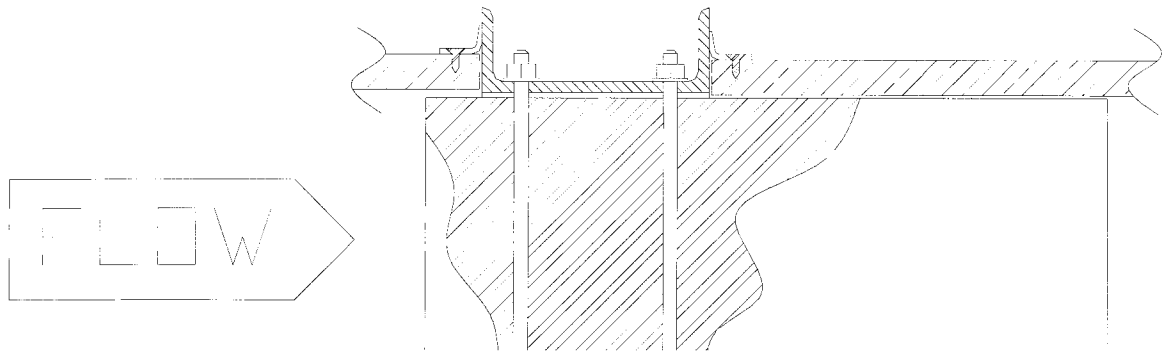


Figure 10: A partially cutaway top view of the proposed vortex generator mechanism.

A mechanism is proposed to actuate the generator, in which springs are preloaded such that the vortex generator can be “fired” to release this preload (Figure 11). The neutral position of the springs can be carefully placed for desirable dynamic characteristics, and the mechanical arrangement can be such that a linear actuator can be used to easily reload the system, allowing automation.

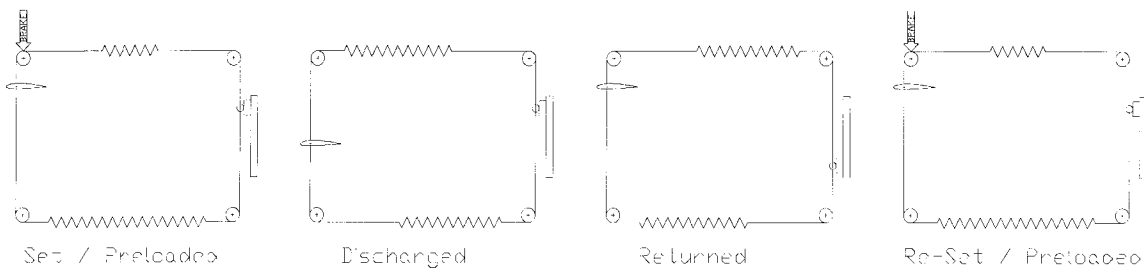


Figure 11: The proposed one degree of freedom mass/spring plunging airfoil vortex generator.

A dynamic analysis of the proposed mechanism has been performed. The free body diagram for the dynamic analysis is shown in Figure 12.

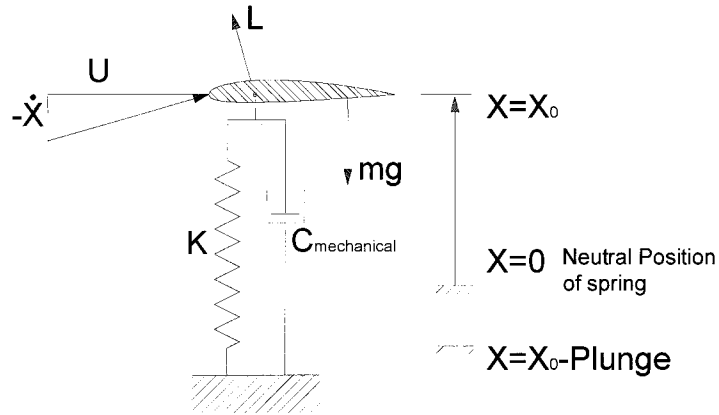


Figure 12: Free Body Diagram of the proposed 1DOF system.

The equation of motion of the above system is:

$$m\ddot{x} + c\dot{x} + kx = -mg - L \cos \alpha \quad (2.2)$$

where:

$$\alpha = \tan^{-1}\left(\frac{-\dot{x}}{U}\right) \quad (2.3)$$

$$L = \frac{1}{2}\rho(U^2 + \dot{x}^2)\frac{\partial C_l}{\partial \alpha}\alpha \quad (2.4)$$

Assuming that $\dot{x} \ll U$, the above linearizes readily to:

$$\alpha = \frac{-\dot{x}}{U} \quad (2.5)$$

$$m\ddot{x} + c\dot{x} + kx = -mg - \frac{1}{2}\rho U \frac{\partial C_l}{\partial \alpha} \dot{x}$$

or:

$$m\ddot{x} + \left[\frac{1}{2}\rho U \frac{\partial C_l}{\partial \alpha} + c \right] \dot{x} + kx = -mg \quad (2.6)$$

The effects of friction are caught up in the parameter c . It is important for this generally non-linear term to be as low as possible, so implementation should include roller bearing linear guide rods of some sort.

Eq. 2.6 was programmed using MATLAB. A variety of spring constants, neutral positions, and low damping coefficients, C , were tested. C and L were found to have little noticeable effect on the dynamics of the system, given the relatively high shifting forces.

The angle of attack required to reach a circulation of 3.22 m²/s (which is to be derived in the next section) was calculated. It was computed that a final angle of attack of ~2.2 degrees would provide the desired circulation. The spring constant, and relationship between the neutral position of the spring and final stop position of the vortex generator were tuned to provide this result, $X_0=0.3$ m, $K=1300$ N/m, with a plunge distance of 0.394 m. The preload force is therefore 390 N, equivalent to only 40 kg. A plot of the time varying velocity is shown in Figure 13. Of note is the approximate constancy of the velocity in the terminal region of the generator's travel.

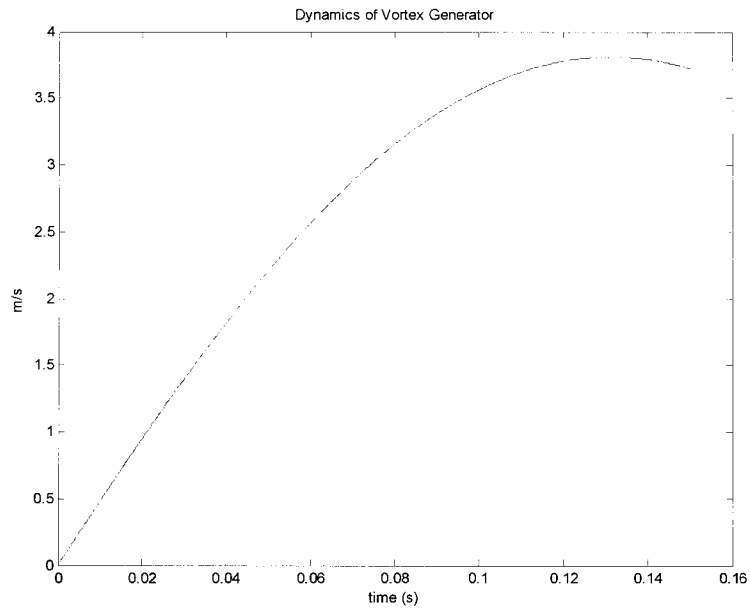


Figure 13: The velocity as a function of time of the 1DOF system represented by the proposed vortex generator.

Also, this design provides vortices of similar circulation, regardless of the free stream velocity, to the threshold of validity of the linearization made in eq. 2.5. As the free stream velocity drops, the effective angle of attack provided by the plunge increases linearly, for reasonably small angles of attack.

2.2 The Test Chamber

In order for the vortex generator to behave remotely like the 1 DOF system shown previously, beam-bending and dynamic motion of that mode in the spar must be, to the greatest extent possible, eliminated. The obvious way to achieve this is to make the spar as stiff as possible. A less obvious method is to make the spar very short. It was decided to investigate the feasibility of a tall, narrow test section, which also maximizes flow

speed without requiring an overly large or expensive fan or blower. A tall, narrow test section must be investigated thoroughly to ensure wall effects do not compromise the experiments.

The test section originally considered to achieve the 100 m/s freestream velocity is profoundly 2-D, having a height of 0.635 m (25 in), and a depth of 0.127 m (5 in). The section has a length of 1.8 m (6 ft). This cross sectional area allows 86 m/s flow from a commercial centrifugal blower delivering 17,000 ft³/min, or 8.06 m³/s, the largest off the shelf unit which meets the space constraints, which will be discussed in the next chapter. Higher flow rates would require the use of a custom built air handling unit, at prohibitive cost. The first proposed test section is shown in Figure 14.

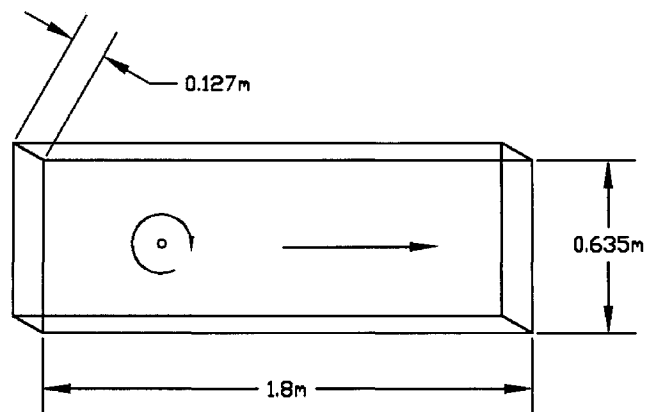


Figure 14: Schematic view of the proposed test section.

A complete air line diagram of the current tunnel appears at the end of chapter 4.

2.2.1 Inviscid Wall Effects

A simple visualization of the flow can be drawn from potential flow theory. An unconstrained vortex has the simple stream function:

$$\Psi = \frac{\Gamma}{2\pi} \ln(\sqrt{x^2 + y^2}) \quad (2.7)$$

In order to constrain the flow, an alternating, infinite series of vortices of equal and opposite circulation must be displaced in the vertical dimension (y) by the height of the test section. This is closely approximated by one vortex above, and one vortex below, providing the stream function:

$$\Psi = \frac{\Gamma}{2\pi} \left[\ln(\sqrt{x^2 + y^2}) - \ln(\sqrt{x^2 + (y+h)^2}) - \ln(\sqrt{x^2 + (y-h)^2}) \right] \quad (2.8)$$

Eq. (2.8) effectively simulates boundaries located where the walls of the test section will lie.

Visualization done in Maple 6, using the actual test section height and vortex strength as initially designed, illustrates this well (Figure 15 & Figure 16). The design circulation for the proposed tunnel is, as mentioned, 3.22 m²/s, and the test section height is 0.635 m.

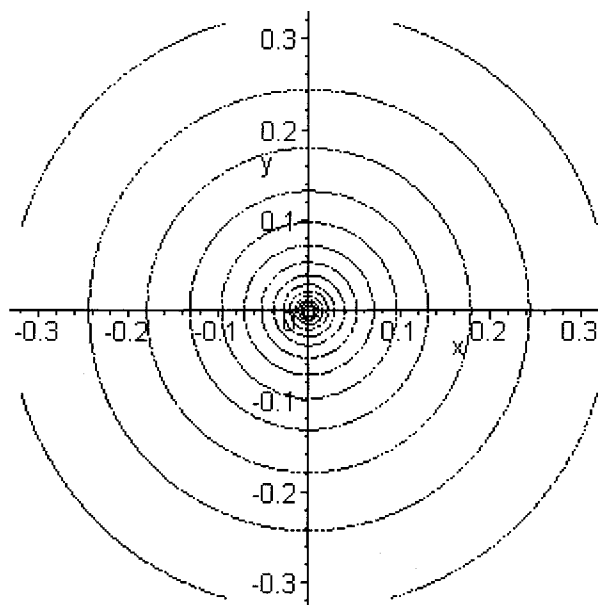


Figure 15: An unconstrained, inviscid vortex of circulation $3.22 \text{ m}^2/\text{s}$.

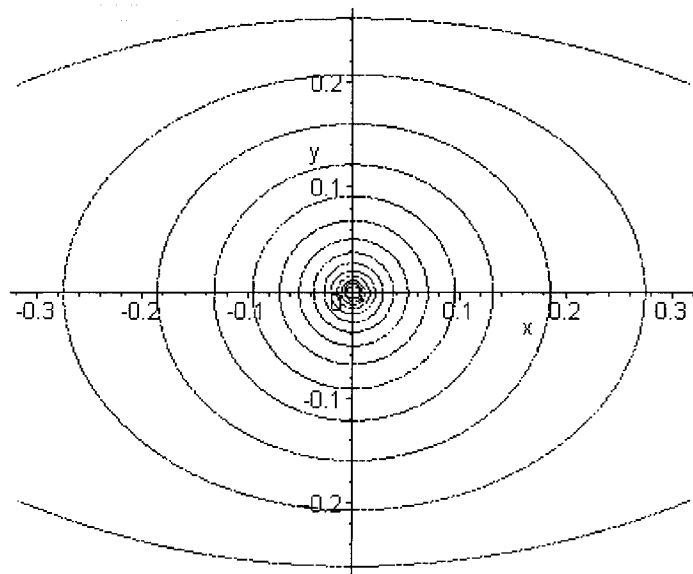


Figure 16: A constrained, inviscid vortex of circulation $3.22 \text{ m}^2/\text{s}$ constrained by walls at $\pm 0.3175 \text{ m}$.

It can be seen from Figure 15 & Figure 16 that the streamlines for the constrained and unconstrained vortices remain quite similar out to roughly 0.2 m radius, or 0.4 m diameter, about 60% of the test section height. This is an intuitively very reassuring result. A target airfoil having a 0.3 m chord will have a thickness of roughly 0.036 m, far smaller than this region of relatively unconstrained flow.

2.2.2 Viscous Wall Effects

The growth of boundary layers in a narrow test section as discussed here should result in the more rapid prominence of wall effects from boundary layer growth. Assuming a boundary layer with a 1/7 power profile, per the well known Blasius method (Fox & MacDonald, 2000), the thickness of the boundary layer at the exit of the test section was calculated using a flat plate description of the test section, due to Blasius:

$$\delta = 0.382 \left(\frac{\nu}{U} \right)^{\frac{1}{5}} x^{\frac{4}{5}} \quad (2.9)$$

and the displacement thickness was determined from:

$$\delta^* = \int_0^{\infty} \left(1 - \frac{u}{U} \right) dy \quad (2.10)$$

The boundary layer thickness was found to be about 2.5 cm, and the displacement thickness 3.3 mm. This displacement thickness would cause the centerline velocity to rise from 100 m/s to 105.9 m/s. Hence, it is suggested that the top wall of the test section be capable of being sloped slightly outward to correct for this velocity increase. The action of the sharp radius at the outlet of a contraction is to substantially shrink the boundary layer, as will be discussed in the next chapter, so much so that it is hopefully

negligible (Mehta & Bradshaw, 1979). This will leave about 7.5 cm of undisturbed “unbounded” flow though the center of the test section, given the ~2.5 cm thick boundary layers on both side walls at the outlet.

2.2.3 Viscous Vortex Behaviour

It is important to realize that the inviscid description of a vortex is only useful outside of the vortex core, in much the same way as inviscid codes provide useful results only outside of boundary layers. The initial size of the vortex core has been observed previously (Strauss et al, 1988) as being roughly twice the thickness of a oscillating type vortex generator’s airfoil. In order to predict the growth in vortex core diameter, a simple derivation was carried out.

The derivation of the time varying behaviour of a viscous vortex growing from a singularity of vorticity can be derived directly from the Navier-Stokes equations applied in the tangential direction in a cylindrical coordinate system:

$$\rho \left(\frac{\partial V_\theta}{\partial t} + V_r \frac{\partial V_\theta}{\partial r} + \frac{V_\theta}{r} \frac{\partial V_\theta}{\partial \theta} + \frac{V_r V_\theta}{r} + V_z \frac{\partial V_\theta}{\partial z} \right) = \rho g_\theta - \frac{1}{r} \frac{\partial p}{\partial \theta} + \mu \left\{ \frac{\partial}{\partial r} \left(\frac{1}{r} \frac{\partial}{\partial r} [r V_\theta] \right) + \frac{1}{r^2} \frac{\partial^2 V_\theta}{\partial \theta^2} + \frac{2}{r^2} \frac{\partial V_r}{\partial \theta} + \frac{\partial^2 V_\theta}{\partial z^2} \right\}$$

Assuming:

$$\text{Axial symmetry } \therefore \partial/\partial\theta = 0; \quad \partial p/\partial\theta = 0$$

$$\text{Zero radial pressure gradient } \therefore V_r = 0$$

$$\text{Homogeneity in Z } \therefore V_z = 0; \quad \partial/\partial z = 0$$

Thus,

$$V_\theta = V_\theta(r, t)$$

So the simplified equation becomes

$$\frac{\partial V_\theta}{\partial t} = \nu \left(\frac{\partial}{\partial r} \left(\frac{1}{r} \frac{\partial}{\partial r} [r V_\theta] \right) \right) \quad (2.11)$$

Taking advantage of the relationship between circulation (Γ), and tangential velocity (V_θ)

$$\Gamma = 2\pi r V_\theta \quad \text{or} \quad V_\theta = \frac{\Gamma}{2\pi r}$$

(2.11) can be written as

$$\begin{aligned} \frac{1}{2\pi r} \frac{\partial \Gamma}{\partial t} &= \frac{\nu}{2\pi} \left(\frac{\partial}{\partial r} \left(\frac{1}{r} \frac{\partial}{\partial r} \Gamma \right) \right) \\ \frac{\partial \Gamma}{\partial t} &= \nu \left(\frac{\partial^2 \Gamma}{\partial r^2} - \frac{1}{r} \frac{\partial \Gamma}{\partial r} \right) \end{aligned} \quad (2.12)$$

Defining a coordinate transform in aid of a similarity solution:

$$\Gamma = f(\eta) \quad \text{where: } \eta = \frac{r}{\Delta} \quad \text{and } \Delta = \Delta(t)$$

$$\therefore \frac{\partial \Gamma}{\partial r} = \frac{f'}{\Delta}; \quad \frac{\partial^2 \Gamma}{\partial r^2} = \frac{f''}{\Delta^2}; \quad \frac{\partial \Gamma}{\partial t} = -f' \frac{r}{\Delta^2} \frac{\partial \Delta}{\partial t}$$

and performing the substitution, multiplying through by r^2 , the LHS by $\frac{\Delta}{\Delta}$ gives:

$$-\eta^3 f' \Delta \frac{\partial \Delta}{\partial t} = \nu (\eta^2 f'' - \eta f')$$

Setting:

$$\Delta \frac{\partial \Delta}{\partial t} = \nu$$

and integrating to determine the expression for the time dependent vortex core size, one can obtain

$$\Delta = \sqrt{2\nu} \quad (2.13)$$

This leaves a the second order, linear, homogenous, ordinary differential equation:

$$f'' + \left(\eta - \frac{1}{\eta} \right) f' = 0 \quad (2.14)$$

This second order differential equation is in fact a simple first order differential equation

in f' , as $f'' = \frac{\partial f'}{\partial \eta}$ and so can be can be solved by separation of variables.

$$\frac{\partial f'}{\partial \eta} = \left(\frac{1}{\eta} - \eta \right) f'$$

$$\frac{1}{f'} \partial f' = \left(\frac{1}{\eta} - \eta \right) \partial \eta$$

Integrating both sides yields

$$f' = \eta e^{-\frac{\eta^2}{2}}$$

Integrating again results in

$$f = C - e^{-\frac{\eta^2}{2}} \quad (2.15)$$

This shows that the time similar circulation distribution, in the radial direction, is a standard normal distribution. Substituting back into the original coordinates;

$$\Gamma(r, t) = \Gamma_i \left(1 - e^{-\frac{r^2}{4\nu t}} \right) \quad (2.16)$$

$$\therefore V_\theta(r, t) = \frac{\left[\Gamma_i \left(1 - e^{-\frac{r^2}{4\nu t}} \right) \right]}{2\pi r} \quad (2.17)$$

A comparison of the circulation and velocity profiles of viscous and inviscid vortices is shown in Figure 17.

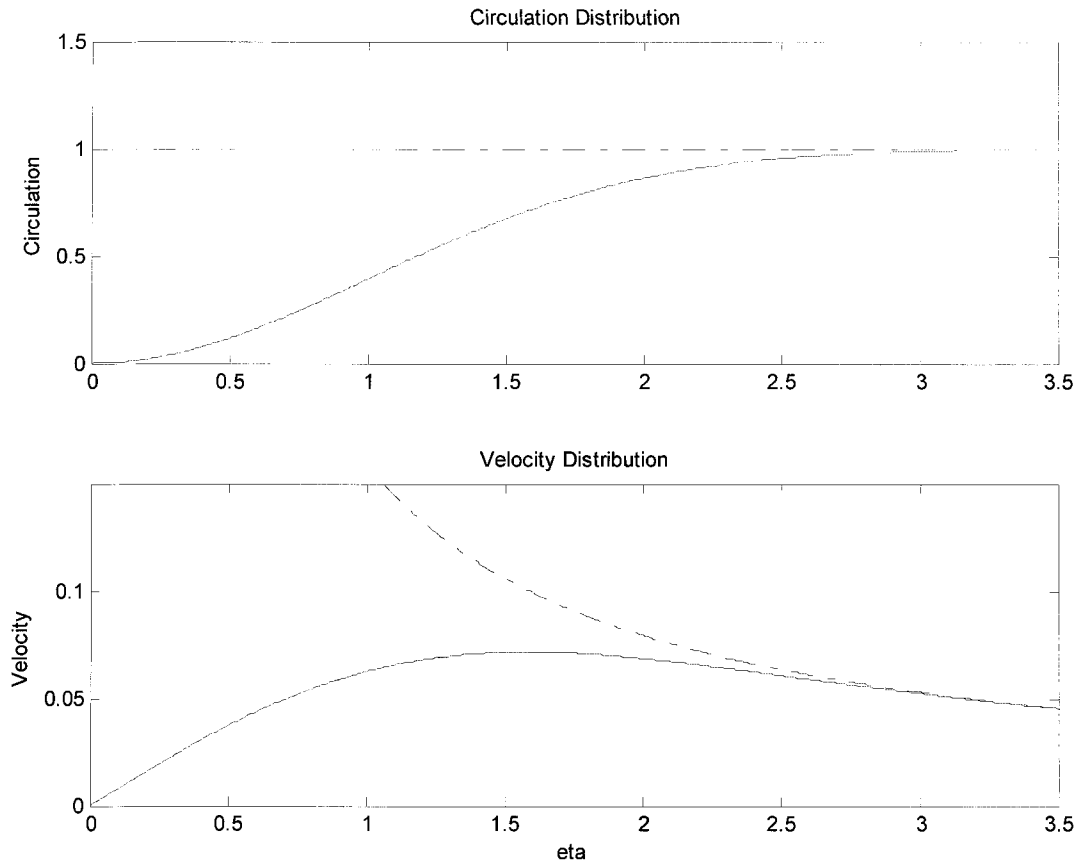


Figure 17: Viscous (solid) and Inviscid (dashed) values of circulation and tangential velocity expressed in terms of normalized radius $(r/(2vt)^{1/2})$.

Choosing $\eta=3$ ($\eta = r/(2vt)^{1/2}$) as the point at which the viscous vortex begins to behave essentially as an inviscid vortex, it can be shown that in the time the vortex is convected at 100 m/s across 1.8 m, the length of the test chamber, the vortex core will have grown by only 0.00023 m, from Eq. 2.13. If the vortex core diameter as it is created by the vortex generator is taken to be on the order of the thickness of the airfoil section (Strauss

et al., 1988), this growth is inconsequential. Thus, to consider wall effects in an inviscid fashion seems valid.

2.3 Evaluation of Similarity Parameters

In the study of BVI, it would be ideal to identify a set of non-dimensional parameters which would simplify prediction. The simplest criteria for evaluation are the Reynolds number and Mach number of the model in the wind tunnel (in this case that of the target airfoil).

In the interests of maximizing dynamic similarity, it would be ideal to use actual size helicopter rotor blades, which have a typical chord length of 30 cm. Unfortunately, this would require a flow velocity of about 250 m/s. At this speed, the tunnel would be a rather expensive and potentially dangerous pressure vessel, with fan requirements far greater than feasible. It seems prudent to try to approach dynamic similarity, within some reasonable limit.

The circulation of the vortices occurring in actual rotorcraft can be estimated from a very simple analysis. A helicopter in level flight or at a constant rate of descent produces an amount of lift roughly equal to its weight. This number divided by the number of blades, yields the lift per blade. From Kutta-Joukowski law,

$$L = \rho U_{\infty} \Gamma \quad \text{or} \quad \Gamma = \frac{L}{\rho U_{\infty}} \quad (3.18)$$

a two dimensional value for the circulation can be calculated. Obeying the well-known rule of thumb that 50% of the bound vorticity of a wing is shed as a stable tip vortex (Caradona *et al*, 1988), this number should be divided by two, and has been used as a target figure for the proposed tunnel. The aircraft considered in this derivation was a Bell 407 weighing 22,250 N, with four blades. These values provide an estimated circulation of 3.22 m²/s.

Some similarity in the ratio of vortical Reynolds number (Γ/ν) to dimensional Reynolds' number of the target airfoil would have been entirely adequate. Instead, as shown previously, the proposed tunnel will provide nearly three times the level of circulation to free stream velocity, thus providing greater experimental flexibility.

2.4 Design Modification

A concern, based on examination of Figure 13 is that the vorticity shed by the vortex generator while it is first accelerating could form an unsteady region of swirled flow immediately preceding the cohesive vortex provided by the sudden stopping of the airfoil. For this reason, it was decided to extend the height of the test section from 0.6350 m to 0.7366 m, and include a flat plate flow separator 0.1016 m from the top wall. This reduces the design velocity from 100 m/s to 86 m/s but is seen as an acceptable compromise, given that the expression of dynamic similarity with respect to circulation is the selected similarity parameter. Also, 86 m/s remains quite a generously fast low speed wind tunnel in which to expect to achieve successful vortex generation.

2.5 Instrumentation

Once the flow conditions required to accomplish the experiment are arranged, new difficulties with respect to the collection of data arise. The flow speed of 86 m/s also means an extremely short duration for the AVI, which implies that ultra high frequency unsteady data collection becomes necessary. High frequency transducers can only gather data at the highest frequency at which they can be polled by an analog to digital converter. Particle Image or Laser Doppler Velocimetry systems which are classified by their manufacturers as high speed, are in fact glacially slow compared to hot wire probes. However, the ability of PIV to take a snapshot of the entire flow field is very much desirable for AVI study. It is hoped that the repeatability of the proposed vortex generator will be so high that subsequent “time steps” of an AVI can be recorded using successive activations of the system.

For this reason, PIV has been selected as a key method of gathering data in the proposed tunnel, in addition to pressure tap measurements around the target airfoil. The gathered data will be used to assemble a characterization of a blade vortex interaction, or some test matrix of Blade Vortex Interactions.

3. WIND TUNNEL DESIGN REVIEW

This chapter will review the design rules for low speed wind tunnels. It is based mostly on information detailed by, or referenced through, the excellent website of Professor Peter Bradshaw and Dr. Rabi Mehta (2003), available at <http://vonkarman.stanford.edu/tsd/pbstuff/tunnel/>.

A wind tunnel can either be an open circuit or a closed circuit type. If the tunnel is a complete ducted-in loop, it is termed “closed circuit”. If the tunnel opens at any point, essentially using the laboratory as part of the return path, it is termed “open loop”. This review will discuss closed circuit tunnel design exclusively, as those rules are easily generalized to cover open circuit designs. In the present work, a closed loop design was selected, as it is intended to install a PIV system in the tunnel, and it is undesirable to intrude on other research taking place in the same laboratory with volumes of waste seeded PIV smoke.

There are eight main components in a closed circuit wind tunnel; 1) a wide angle diffuser, 2) a settling chamber, 3) screens, 4) a contraction, 5) a test chamber, 6) diffusers, 7) corners, featuring turning vanes, and 8) a fan or blower. The numbers correspond to Figure 18:

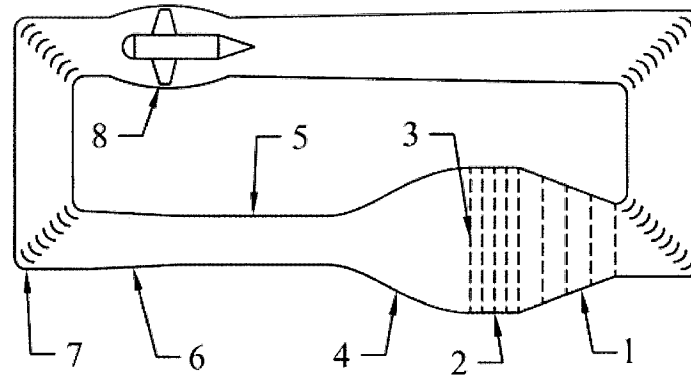


Figure 18: A schematic of a typical closed circuit wind tunnel

The design rules for each of these areas will be briefly reviewed in the order numbered in Figure 18, for convenience. It is important to note that wind tunnel design is a highly iterative process. Design details have enormous upstream and downstream consequences. It is customary in wind tunnel design to treat losses as if they were occurring in any duct system, using the well known loss calculation methods for internal flows, such as HVAC systems (Fox & MacDonald, 2000).

3.1 The Wide Angle Diffuser (WAD)

The Wide Angle Diffuser (WAD) is inappropriately named, as it is not in place to reduce losses by encouraging pressure recovery, as in a normal diffuser, but rather is in place to prevent gross separation of the flow, and keep re-circulations out of the settling chamber (Bradshaw & Mehta, 2003, Mehta & Bradshaw, 1979). Pressure recovery is generally negligible. The ideal shape for the diffuser would consist of curved walls, tangent to the intended direction of flow at the inlet and outlet, but this is difficult in the

extreme to implement. It is common practice to place screens along the length of the contraction, to prevent flow separation, in such a radically angled diffuser.

Screens in the diffuser have a beneficial role in preventing flow separation, (Mehta 1985), as will be discussed in section 3.3. Mehta and Bradshaw (1979) provide design charts (Figure 19 & Figure 20), which show that for this arrangement two screens are adequate for successful operation.

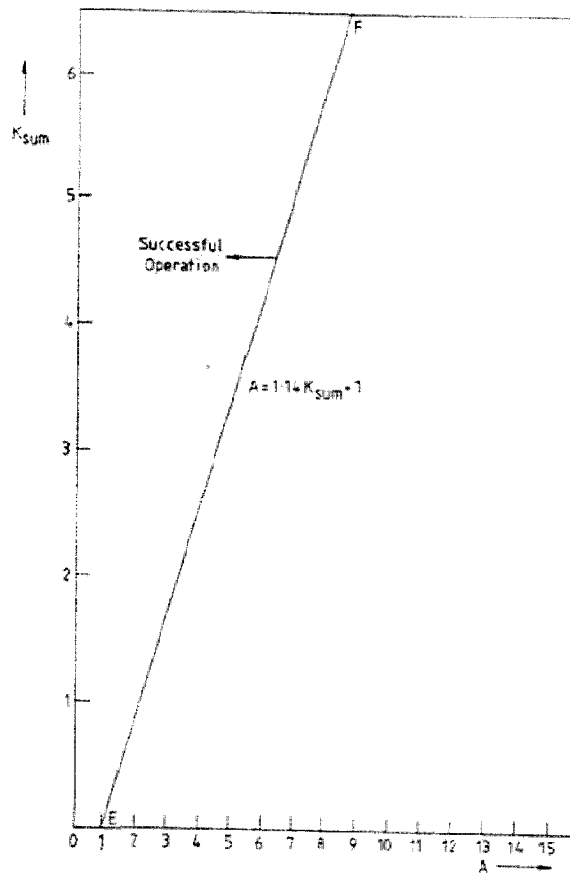


Figure 19: Overall Pressure drop coefficient (K_{sum}), the sum of all the pressure drop coefficients for the screens installed in the WAD, vs. area ratio (A) of the WAD for a diffuser with screens (Mehta & Bradshaw, 1979).

Figure 19 shows a correlation between the total pressure drop coefficient (K_{sum}) in a WAD, and its area ratio, or ratio of outlet area to inlet area.

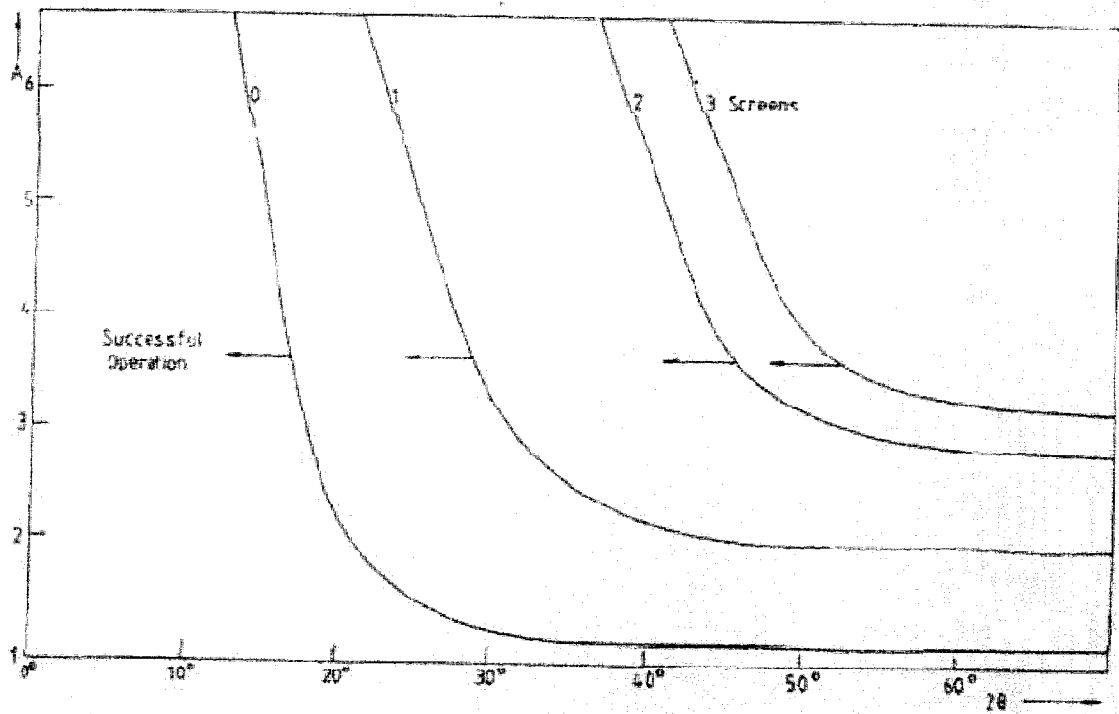


Figure 20: Design Boundaries for diffusers with screens (Mehta & Bradshaw, 1979).

Figure 20 correlates the number of screens in a Wide Angle Diffuser with its included angle, 2θ . The included angle is calculated as the angle between the divergent walls of a circular section diffuser having the same length and area ratio as the rectangular-section diffuser.

The WAD is necessary, as the flow quality needed in the test chamber requires the presence of a contraction and many screens in the flow upstream, all of which operate better for having a region of low flow speed just prior to the contraction. The benefits due to the screens is discussed in section 3.3, and due to the contraction in Section 3.4.

The losses in the WAD generally represent a large fraction of the losses throughout the system, and are best estimated as the full dynamic pressure change over the length of the WAD, plus the losses due to screens necessary to prevent separation. This results

in losses similar to those due to of separation, without the negative consequences to flow in the test chamber associated with separation (Mehta & Bradshaw, 1979).

3.2 The Settling Chamber

The role of the settling chamber is to reduce flow non-uniformities. For this, the flow is passed through several screens in an area where the flow is somewhat slower, so that the beneficial action of the screens does not result in excessive losses. Since a settling chamber long enough for turbulent fluctuations to die out or long enough for flow stabilization to occur due to viscous effects would be unworkably long, the settling chamber is designed as the simplest possible smooth, rectangular duct in which screens can be securely clamped. It is customary to ignore losses due to skin friction in the settling chamber, and only consider the losses across screens within the chamber (Mehta & Bradshaw, 1979).

3.3 The Screens

The screens are capable of two distinct beneficial actions. They simultaneously reduce non-homogeneities in the cross sectional velocity profile of the flow, and diffract the flow towards the normal direction of the screen (Mehta, 1985).

The mechanism by which a screen reduces non-homogeneity is simple. The drag on an obstruction is proportional to the square of the speed of the flow it is placed in. Since a screen is a homogenous obstruction, when it is placed in a non-homogenous flow,

more drag is exerted by higher velocity regions of that flow than by low-velocity regions of the flow. According to Newton, that drag force must be simultaneously exerted on the fluid, also. Thus regions of higher speed are subjected to a deceleration, as compared with regions of lower speed, which are actually accelerated, in order to achieve continuity of mass flow. The pressure gradient across the screen is insufficient to maintain higher speed regions of flow at the original speed, thus, it is slowed. However, the gradient is more than sufficient to carry lower speed regions, so they accelerate (Mehta, 1985).

In order to understand the mechanism by which the screen acts to straighten, or diffract towards the normal, the flow, it is useful to invert the classical picture, and imagine a screen placed in a uniform flow at some angle, rather than a flow approaching at some angle to a vertical screen, as in Figure 21:

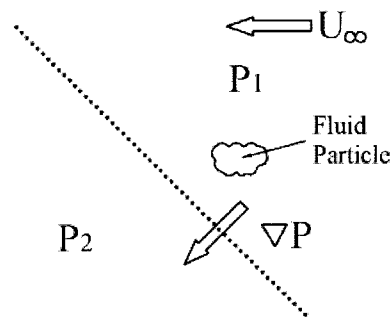


Figure 21: Flow in the region of a screen, placed in the flow at an angle.

As the screen, represented by the dotted line in Figure 21, represents an obstruction, there must be some pressure drop across it. Since the flow at the bottom encounters the screen earlier, then the pressure towards the bottom must be generally lower than flow towards the top. Therefore, a downward component is added to the

general pressure gradient in the region of the fluid particle, causing it to accelerate downward, towards the outward normal of the screen surface.

This flow straightening effect of screens has come to totally replace the “honeycomb”, in classical wind tunnel design (Bradshaw & Mehta, 2003). The addition of a honeycomb to a flow was intended to provide this same flow-straightening effect, but in fact does nothing. From the standpoint of the flow, the honeycomb is a flat plate placed in the flow, and generally, any angularity of the flow with respect to the honeycomb causes it to immediately stall, creating more problems, and solving none. In order for the flow to pass properly through the honeycomb it must have already been substantially straight. In the opinion of the author, it is interesting to ponder the number of failed wind tunnel designs which might in fact be successful, were this “flow improving” device removed.

Losses across screens have been calculated in a number of different ways, the most consistent of which is that due to Wieghardt (1956), who gives the coefficient of loss as:

$$K = 6.5R_e^{-\frac{1}{3}} \frac{(1-\beta)}{\beta} \quad (3.1)$$

Where β is the ratio of open area to total area of the screen, and R_e is Reynolds number as defined by Weighardt for screens:

$$R_e = \frac{Ud}{\nu\beta} \quad (3.2)$$

Where U is the free stream velocity, and d is the diameter of the wire used to make the screen. This provides an expression for the total losses, for all screens in the wind tunnel:

$$h_{l(\text{screens})} = \frac{1}{2} \sum_{n=1}^4 K_n U_n^2 \quad (3.3)$$

3.4 The Contraction

The general purpose of a contraction in a wind tunnel is to accelerate the flow to the working test section velocity, and to reduce stream-wise velocity non-uniformities. The non-uniformities, expressed as a percent of the mean free stream velocity, reduce roughly by a factor $1/A^2$, where A is the area ratio of the tunnel (Mehta & Bradshaw, 1979).

Wind tunnel contraction design is an area of some controversy. The contraction is utterly crucial to the successful operation of a wind tunnel, and so extensive design and analysis is customary. On the other hand, every contraction placed in service whose design is not decidedly offensive to a reasonably intuitive eye has worked at least adequately. Simply put, contraction is an inherently flow-stabilizing process, as opposed to diffusion, which is a flow disturbing process. So long as a few simple design rules are followed, a successful contraction design should result.

The general design parameters for wind tunnel contractions are reasonably well known (Mehta & Bradshaw, 1979), (Bell & Mehta, 1988). The wall profile should be continuous and smooth, meeting the inlet duct and outlet duct at a tangent. Preferably, this wall profile should have zero first and second derivatives at the inlet and outlet, likely as this provides equipotential lines at the inlet and outlet perfectly orthogonal to the intended direction of flow, i.e. the test chamber centerline. The radius of curvature at the

inlet should be larger than that at the outlet, as the concave radius seen by the flow at the inlet presents an adverse pressure gradient to the flow, and the convex radius at the outlet causes a strong favorable gradient. The adverse gradient will tend to thicken boundary layers, and so should be as gentle as practical, and the favorable gradient will tend to thin them, and so should be as sharp as possible, without risking the formation of a *vena contracta*.

A fifth order polynomial has been identified as ideal for satisfying the condition of zero first and second derivatives at the inlet and outlet by Bell and Mehta (1988), given below as Eq. 4.4, where h/H_i is the non-dimensionalized height from centerline, and ζ is the non dimensional length of the contraction, (x/L),

$$\frac{h}{H_i} = \left[-10(\xi)^3 + 15(\xi)^4 - 6(\xi)^5 \right] \left(1 - \frac{H_o}{H_i} \right) + 1 \quad (3.4)$$

This polynomial has been transformed slightly by Brassard and Ferchichi (2004) to meet the criteria of larger inlet radii than outlet radii, as

$$\eta = 10\xi^3 - 15\xi^4 + 6\xi^5$$

$$\frac{h}{H_i} = \left[-\eta \left(1 - \left(\frac{H_o}{H_i} \right)^{\frac{1}{f(\zeta)}} \right) + 1 \right]^{f(\zeta)} \quad (3.5)$$

Where $f(\zeta)$ is some continuous, smooth function of ζ , most conveniently a constant, as depicted below in Figure 22.

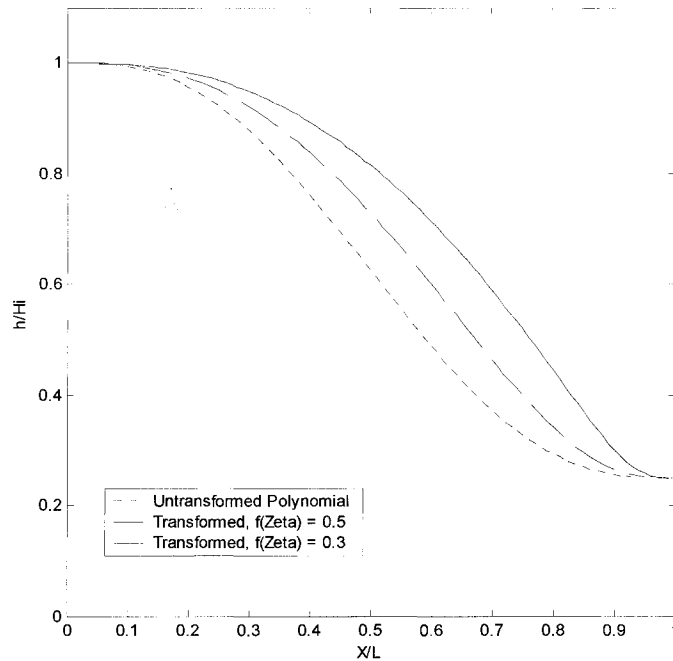


Figure 22: The effect of varying $f(\zeta)$, according to Eq. 3.5.

The effect of this changing $f(\zeta)$ apparently alters primarily the ratio of the inlet radius to the outlet radius and affords the possibility of attempting to optimize the design according to carefully chosen parameters using CFD.

Losses in the contraction are generally negligible. 1/3 of the contraction length is sometimes added to the test chamber length during loss calculation for that region (Bradshaw, 2004).

3.5 The Test Chamber

There is no generic test chamber to describe, as each is specific to the type of experimentation intended. It is important to mention that boundary layer growth in the test section will tend to result in a pressure gradient in the mean flow. It is therefore

useful to have as a minimum one adjustable wall, generally the top wall, so the cross sectional area can be adjusted longitudinally, and correct for this. Unfortunately, the only method to achieve this correction is tedious trial and error.

Losses in this region should be calculated using any reasonable flat plate relation for skin friction drag, treating the test chamber as if it had been “folded open”, and placed in an unbounded flow. Once the skin friction has been integrated over the equivalent area of all four walls to provide a total drag force, the pressure difference across the cross section of the test chamber which would create that same drag force is simple to calculate. This is the pressure loss in the test chamber.

3.6 Diffusers

Unlike the WAD, diffusers placed in the return path are intended to behave as classical diffusers; they promote pressure recovery, and discourage separation (Bradshaw & Mehta, 2003). The included angle, that is, the angle between the walls of a circular section diffuser having the same length and area ratio of the polygonal diffuser being designed, should be kept to less than 5 degrees. If this can be done, then it is hopefully safe to assume that pressure recovery is complete, so no losses due to diffusion occur. The friction losses can be estimated using the familiar relations due to Moody for fully developed turbulent flow. While the flow is unlikely to be fully turbulent exiting the test section, once the first corner has been passed, it most certainly will be.

3.7 Corners and Turning Vanes

In closed circuit wind tunnels, corner vanes are required to prevent flow separation in the corners, as will happen with all but the gentlest plain bends (Bradshaw & Mehta, 2003).

Corner vanes are often the subject of considerable design and analysis, given how crucial they are to relatively low levels of losses in the return path. Researchers have employed complex design techniques to reduce corner losses while maintaining minimal wind tunnel dimensions (Lindgren & Johansson, 2004).

These heroic design efforts, and no doubt enormous construction costs, are necessary only if optimal aerodynamic performance is being emphasized unnecessarily. If loss reduction is taken as the principal method of reducing costs, in the form of a less expensive fan or blower, designers can easily (and unfortunately) ignore another route to economy; a more expensive or larger fan or blower, but a much more economical design and construction phase for the tunnel. Precisely designed and fabricated airfoil-sectioned corner vanes, evaluated using CFD and produced at ruinous cost can decrease the corner loss coefficients generously (Sahlin & Johansson, 1991). Lindgren and Johansson (2004) quote pressure drop coefficients of as little as 0.047, an astonishing result, given that the pressure loss coefficients range from 0.12 to 0.15 for rolled sheet (Bradshaw & Mehta, 2003).

The engineering reality is that the design and procurement of more than a hundred precisely manufactured airfoils, and their laborious fitting into the corner frames would be more costly in money and time than could possibly be saved in horsepower

requirements at the blower. It seems the best course that simple sheet metal vanes be roll formed, and fastened into the corners.

The current design procedures for these types of corner vanes are again well known (Bradshaw & Mehta, 2003). A gap to chord ratio of 0.25 is recommended, and the vanes should have circular chords, enclosing 85-86 degrees. The leading edges should be at around 4 degrees of angle of attack, and the trailing edges should be aligned with the flow. A short straight sections at the trailing edge is recommended (Bradshaw & Mehta, 2003).

The losses in the corner vanes should be calculated using $K=0.12-0.15$ (Mehta & Bradshaw, 1979).

It is useful to note that a longer diffuser at the outlet of the test section could substantially reduce the losses in the first corner region, but can be difficult to implement, given space constraints.

3.8 The Fan or Blower

Fan or blower sizing for wind tunnel duty is no different than the selection process for any air handling system. That said, there are important considerations with respect to outlet swirl, inlet conditions, be it via the laboratory, in an open circuit tunnel, or via the ductwork and corner vanes of a closed circuit tunnel. Except in the case of very large wind tunnels, in which a custom built fan is necessary, fan or blower selection is generally an exercise in catalogue selection.

It has been the design standard in the past to use an axial fan placed somewhere in the return path of a closed circuit wind tunnel, usually at the beginning of the long leg of the return path, as shown previously in Figure 18. A relatively new concept due to Professor John Eaton at Stanford University (Bradshaw, 2004) in wind tunnel design is the replacement of one corner vane assembly in a closed circuit tunnel with a centrifugal blower (Figure 23). The general suitability of centrifugal blowers for duty in wind tunnels is well known, as they are very common in open circuit tunnels (Bradshaw & Mehta, 2003).

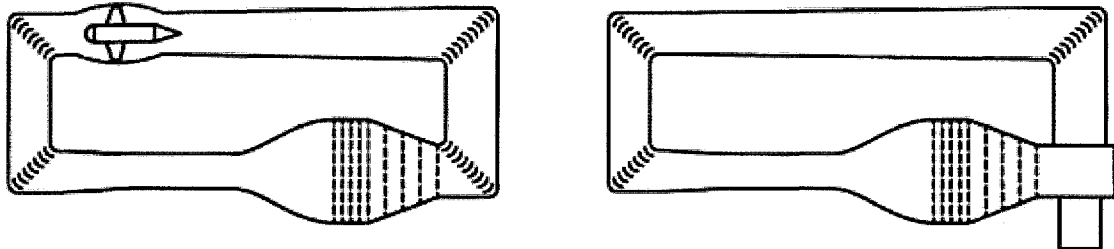


Figure 23: Otherwise identical closed circuit tunnels, one employing an axial fan (left) the other employing a centrifugal blower (right). Note that one set of corner vanes is saved in the blower configuration.

The velocity distribution at the outlet of a centrifugal blower is extremely non-uniform, swirled, and chaotic. The keys to the success of centrifugal blowers in wind tunnel design is the blower's ability to create pressure sufficient to allow the installation of many more screens, and the broader range of system points at which the blower approximates its maximum efficiency. In the case of an axial fan, a change in system point can easily drive the blades into stall, creating profoundly swirled flow at the outlet. A centrifugal fan is largely immune to these effects.

4. IMPLEMENTATION AND TESTING

Throughout this chapter, length dimensions are presented in Imperial units, as those are the units in which construction materials are available. Where such calculations are presented, flow measurements and calculations are performed using metric units, as they are clearly superior for such tasks.

4.1 Design Space

The space available for the new wind tunnel was extremely limited, being a portion of dead area behind an existing wind tunnel, as shown in Figure 24.

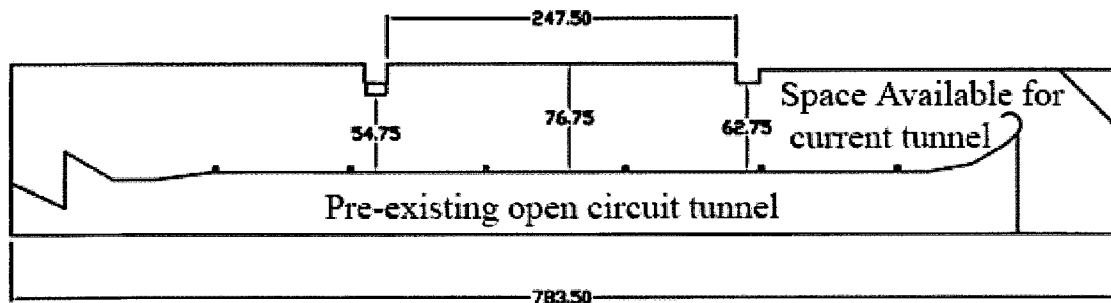


Figure 24: The space available. All dimensions are in inches.

This limited space is clearly insufficient for a classical racetrack type closed circuit wind tunnel, so it was conceived to build the wind tunnel on its side, that is, the return path above the test chamber, as the ceiling is much higher than the space is wide.

Clearly, an off the shelf centrifugal blower cannot operate on its side due to the low thrust capacity of the standard bearings and a gravity tensioned belt drive, nor is

there room to put a relatively large centrifugal air handling unit in place, sideways. Therefore, a “five cornered square” concept was devised (Figure 25 & Figure 26).

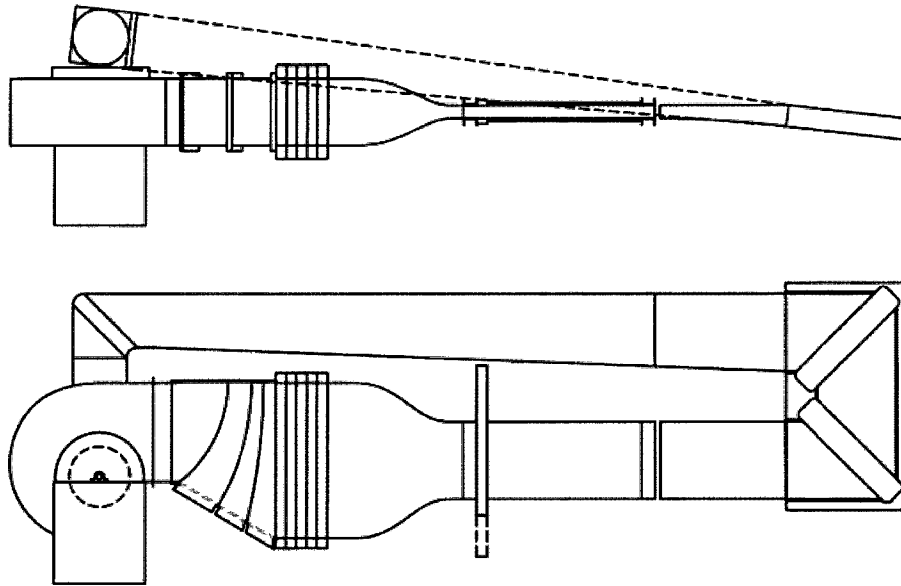


Figure 25: Schematic of the new tunnel concept, side and top views. A fifth corner turns the flow directly into the inlet of the blower.

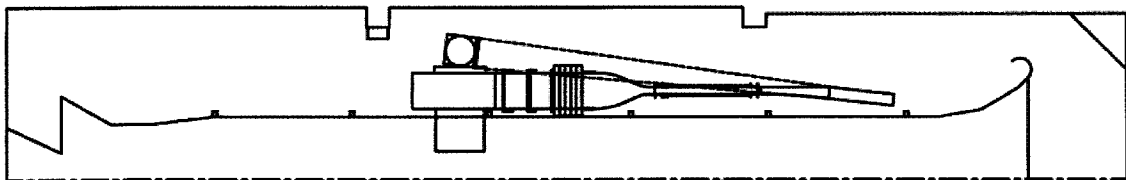


Figure 26: The tunnel placed in the available space.

It is important to note that the “five cornered” geometry loses the benefit of removing one set of corner vanes, but is a necessary design compromise, given that the selected blower (discussed in Section 4.11) weighs roughly one metric ton, and stands 2 m tall.

It is difficult to discuss implementation in a linear fashion, given the highly iterative design process required in wind tunnel design. Though the specific elements of

the wind tunnel will be discussed in the order found in Chapter 3, it is unclear which order to discuss them in. For example, the width of the WAD, settling chamber, and inlet of the contraction was selected as 25", which is the width of the outlet of the blower chosen, a blower which was chosen based on its ability to provide flow to that 25" wide duct. This is purely a matter of construction convenience. It is obviously not the case that the blower was chosen for the size of its outlet. The reader should keep this iterative design process in mind at all times.

4.2 Lab Airflow Impact Study

It is important that new research facilities have as little adverse impact on existing facilities as possible. As the pre-existing wind tunnel is open circuit, radical changes to the lab can negatively affect flow homogeneity inside of the pre-existing tunnel. To determine the effect, if any, a simple experiment was performed.

A plywood cutout having the same dimensions as the largest cross section of the planned tunnel, being the blower and final leg of the return path, was prepared. 20 data points were selected within the pre-existing tunnel test section, roughly 6 feet from the outlet of the contraction, starting 6 inches from the inner walls of the tunnel, and regularly spaced in a 4 high by 5 wide grid. The pre-existing tunnel was run to 55 \pm 0.1 km/hr as indicated by the installed sensors in the tunnel, and velocity readings were taken at each of the grid points using a turbine-type anemometer, an Omega HHF300A, clamped in a test-tube stand. The experiment was performed with the plywood cutout placed in the appropriate area, and removed from the flow entirely. Prior to each series

of tests, the dust screens at the inlet to the tunnel were vacuumed. These results are presented in Table 1 & Table 2.

Table 1: Velocity measurements associated with an unobstructed room, positions are as seen from within the tunnel, looking upstream:

	6"	19.5"	33"	46.5"	60"	Deviations
40"	18.58	17.86	17.56	17.81	17	0.57
28.6"	17.81	17.3	17	17.09	17.36	0.32
17.3"	18.05	17.41	17.05	17.21	17.75	0.41
6"	18.87	18.75	18.45	18.19	19.34	0.44
Deviations	0.48	0.66	0.67	0.52	1.03	

Table 2: Velocity measurements associated with an unobstructed room, positions are as seen from within the tunnel, looking upstream:

	6"	19.5"	33"	46.5"	60"	Deviations
40"	18.06	17.69	17.42	17.48	17.44	0.27
28.6"	17.71	17.06	17	17.01	17.15	0.30
17.3"	17.6	17.21	17.1	17.11	17.64	0.27
6"	19.47	19.04	19.02	18.92	19.23	0.22
Deviations	0.86	0.90	0.94	0.88	0.93	

The standard deviations of the data measurements have been calculated. The measurements taken with an unobstructed room have a standard deviation of 0.69 m/s, and the standard deviation taken with an obstructed room is 0.83 m/s, the difference being just 0.14 m/s, or 0.8% of the mean flow velocity.

More informative perhaps is an analysis of the standard deviations taken of each row and column individually, which are shown at the bottom and right of each row and column in Table 1 & Table 2. The row-wise deviations are uniformly much lower in the obstructed room measurements. Row-wise variation is exactly where negative impacts

of increased room obstruction would be expected. If the obstruction were adversely affecting return flow on the side it exists on, this result would be unlikely. Examination of surface plots of the results is also useful. These are shown in Figure 27 & Figure 28:

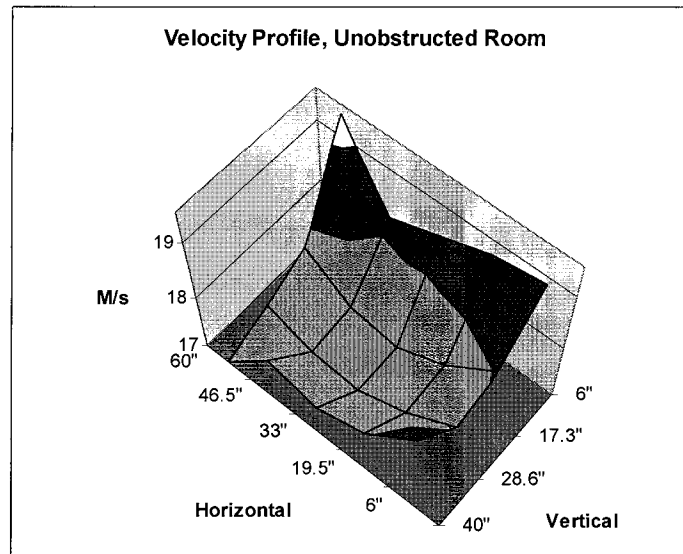


Figure 27: Velocity profile associated with an unobstructed room, shown rotated for clarity.

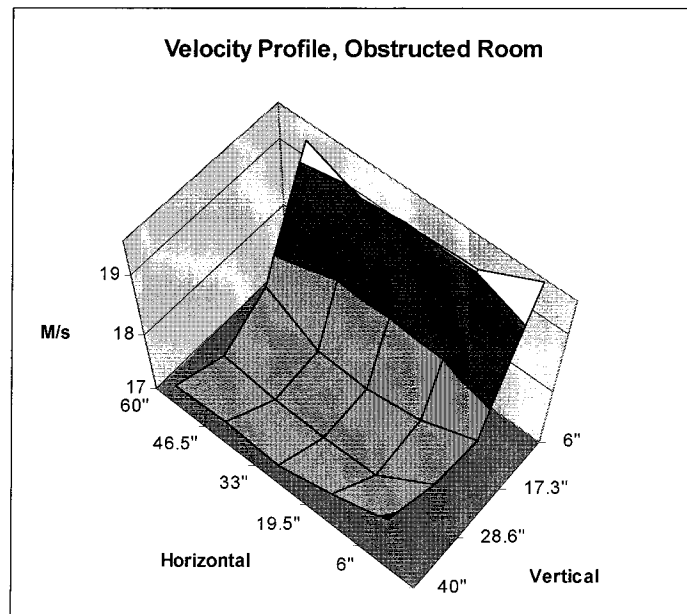


Figure 28: Velocity profile associated with an obstructed room, shown rotated for clarity

It is difficult to argue that either velocity profile would be “better” than the other. It is also obvious that the flow pattern in the obstructed room is highly symmetrical in the horizontal dimension, possibly more so than in the unobstructed room, leading to the conclusion that the obstruction presented by the implementation of the current tunnel is of little or no negative consequence to the flow in the existing tunnel.

4.3 Wide Angle Diffuser (WAD)

The arrangement of the proposed tunnel allows the convenience of a two dimensional diffuser, that is, a diffuser having two parallel walls, 25 inches apart. This simplifies construction greatly. Parallel walls also allow the screens to be installed curved, so that the screen is constantly at advantageous angles to the desired direction of flow.

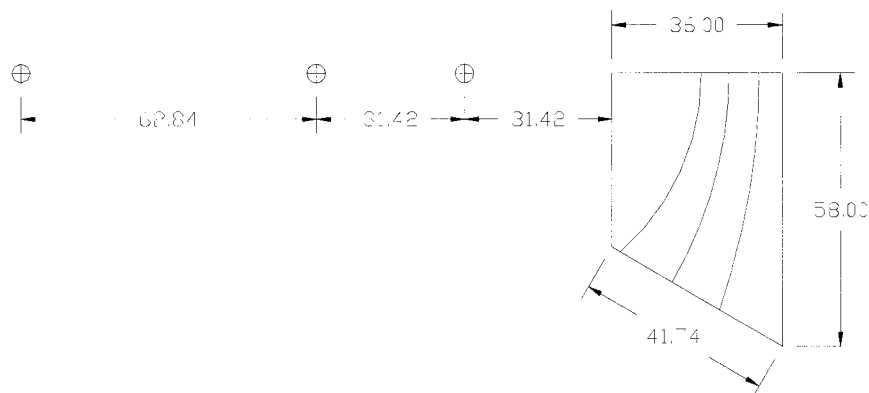


Figure 29: Schematic side view of the diffuser. Curved lines are locations for screens. Crossed circles are the center points for the screen locations depicted (Dimensions are inches).

In Figure 29, it can be seen that the screen insertion locations are not coaxially curved, as one might intuit. The refractive property of screens in a flow, discussed in section 4.3, is used to encourage flow to remain attached to the bottom wall of the WAD (Mehta, 1985). As discussed, screens have a tendency to divert flow towards the surface normal of the screen, at every point over their surfaces. It therefore seemed sensible to vary the radius of the screens so that the transition from straight duct to diffuser and back to straight duct is at least somewhat eased (Bradshaw & Mehta, 2003). This is not an area where calculation is of particular use, as the study of flow through screens, particularly as it pertains to wind tunnel design, involves so many variables as to remain profoundly empirical, and no prudent designer risks designs so adventurous as to provide good failure cases for study.

Adherence to the design rules discussed in section 4.1 indicate successful operation with 4 screens. The diffuser, as implemented is shown in Figure 30.



Figure 30: The Wide Angle Diffuser, as implemented.

4.4 The Settling Chamber

The implemented design involves sections of $\frac{3}{4}$ inch by 4 inch engineered lumber built into frames, also of $\frac{3}{4}$ inch by 4 inch, so that the screens can be mounted in other, very simple frames, which sit external to the join of the sections, as shown in Figure 31. This novel approach simplifies construction greatly, and represents substantial cost savings.

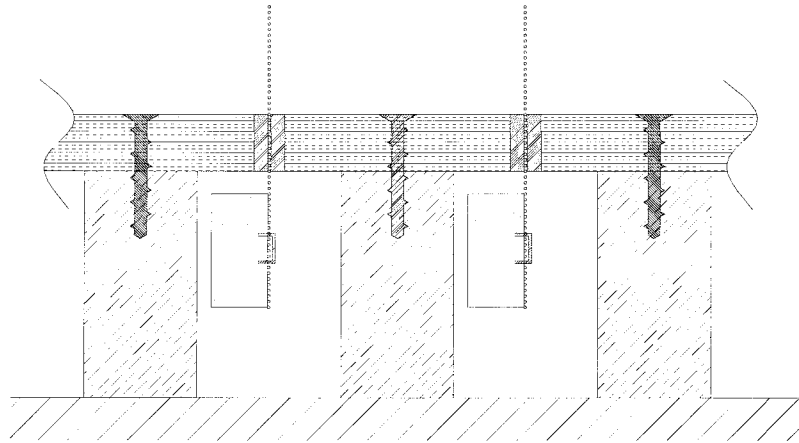


Figure 31: Side view detail of screen mounting method in settling chamber.

Figure 31 clearly shows that the inherent straightness, smoothness, and stability of engineered lumber is being used to excellent effect, as it ensures that the inner walls are flush, with no great effort on the part of the builder. The externally clamped screens are trivial to construct, compared to the traditional method of laboriously clamping the screens into very precisely cut frames, the inner edge of which is exposed to the flow.

It was selected to place 6 screens in the settling chamber. A detail view of the settling chamber, as implemented, is shown in Figure 32.

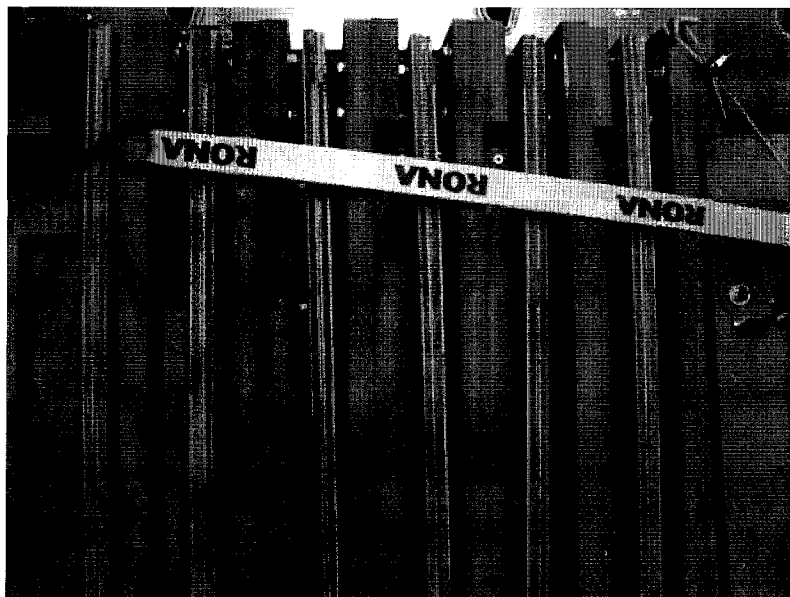


Figure 32: Detail of the Settling Chamber, as implemented.

4.5 Screens

The narrowness of the wide angle diffuser and settling chamber allowed the enormous convenience of off-the-shelf stainless steel wire cloth, made for the food industry, for a very modest cost. In the interest of simplicity, it was decided to use the same mesh density and wire diameter for all the screens. The screen wire diameter and the opening is very similar to common household screen, designed to deter insects.

The screens will accrete oil from the PIV smoke generator over time. The design of the WAD and settling chamber is such that they can be easily removed and cleaned.

4.6 Testing outlet flow from Settling Chamber

In order to evaluate the performance of the WAD, Settling Chamber and the selected screens, purely to predict successful operation of the current tunnel, a simple test was performed. It is presented here in case it may be useful for comparison to subsequent wind tunnel designers. A velocity profile was taken at the outlet of the settling chamber, using the same hand held, turbine-type anemometer, an Omega HHF300A, as used in section 3.1. The profile was taken 3 times, and the results examined for flow homogeneity, and variability between trials (flow steadiness). The results are presented here in Table 3, Table 4, and Table 5.

Table 3: Velocity readings at outlet of settling chamber, in m/s, trial 1.

		Y pos. of probe			
		2"	9"	16"	23"
Z. pos of probe	56"	9.7	9.55	9.71	8.42
	47"	9.47	9.43	9.41	8.17
	38"	9.23	8.97	8.91	7.67
	29"	8.92	8.82	8.77	7.55
	20"	9.62	9.34	9.35	8.21
	11"	9.36	8.38	8.95	8.18
	2"	9.51	9.53	9.46	8.54

Table 4: Velocity readings at outlet of settling chamber, in m/s, trial 2

		Y pos. of probe			
		2"	9"	16"	23"
Z. pos of probe	56"	10.15	9.65	9.96	8.58
	47"	9.41	9.15	9.02	8.21
	38"	9.31	9.03	8.34	7.47
	29"	9.33	9.06	8.84	7.65
	20"	9.58	9.18	9.36	8.16
	11"	9.43	9.14	9.33	8.32
	2"	9.57	9.13	9.59	8.65

Table 5: Velocity readings at outlet of settling chamber, in m/s, trial 3.

		Y pos. of probe			
		2"	9"	16"	23"
Z pos. of probe	56"	9.81	9.61	9.81	8.51
	47"	9.1	8.84	8.79	8.03
	38"	9.25	9.06	8.97	7.73
	29"	9.29	9.14	9.06	7.84
	20"	9.33	9.4	9.4	8.19
	11"	9.36	9.13	9.4	8.21
	2"	9.81	9.25	9.44	8.62

In trial 1, the outlier furthest from the mean is 16%. In trial 2, the outlier furthest from the mean is 17.2%. In trial 3, the outlier furthest from the mean is 14.2%. Given the general characteristic of contractions to reduce stream-wise fluctuations by a factor $1/A^2$, as discussed in section 3.4, the resulting stream-wise fluctuation in the test chamber, for a 10:1 contraction ratio, would be 0.172%, which is respectably low. The standard deviation between all three trials, at each point was taken, to give some idea of the steadiness of the flow. An average was taken of these 28 standard deviations expressed a percentage of the mean reading at that location, and was just 1.69%. The flow at the outlet of the settling chamber appears to be steady, even considering the rough measurements possible with the handheld anemometer.

4.7 Contraction

The dimension of the width of the WAD and settling chamber were chosen to match the width of the outlet of the blower. In fact, there is some small difference between the width of the blower outlet (24.75inches), and the width of the WAD and settling chamber. 25 inches was chosen, as it is exactly five times the width of the test

section discussed in chapter 3.2 (5 inches). Thus, the chosen height of that test chamber (29 inches) need only be doubled to provide a 10:1 contraction ratio. Thus, the inlet of the contraction was chosen to be 25 inches X 58 inches, and the outlet remains 5 inches X 29 inches. The length of the contraction was chosen as 51.5 inches or one hydraulic diameter of the inlet of the contraction (Bradshaw & Mehta, 2003) (Fox & MacDonald, 2000), and an 8 inches straight section at the inlet to allow turbulence from the last screen to decay.

The transformed polynomial due to Brassard and Ferchichi (2004) was chosen for the design process. Using a constant value $f(\zeta)$, it was hoped that the contraction profile could be optimized for thin boundary layers through a CFD analysis using the 2D version of Carleton Multi Block (CMB). For a review of the capabilities of CMB, see Davis *et al.* (2005).

A code was written in Matlab to generate meshes. The lengthwise spacing was constant, with 100 nodes in that direction. The first spacing near the wall was $10^{-7} L$, length being the dimension chosen for normalization, and the expansion factor was 1.155. This resulted in at least 50 nodes inside the boundary layer at the outlet for every case. A sample mesh is shown in Figure 33. The baseline case, a symmetric profile was examined using a first spacing of 5×10^{-8} , and 2×10^{-7} , with 200 and 50 nodes lengthwise, respectively to determine mesh dependence. In all cases, the results were virtually identical.

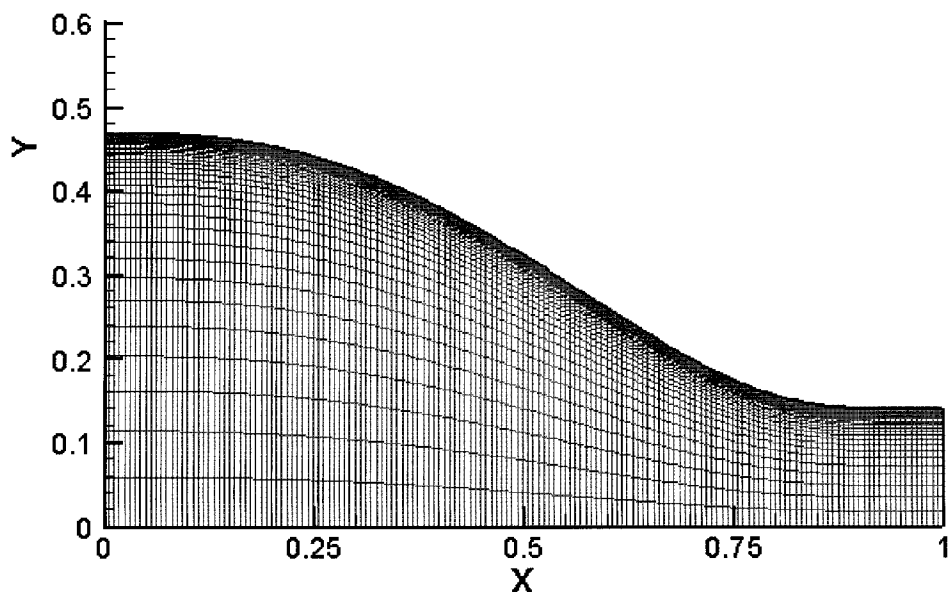


Figure 33: Mesh topology used in the CFD optimization of the contraction.

It was decided to perform a golden section search in an effort to minimize the boundary layer at the outlet of the contraction. It was found that the boundary layers became thinner as $f(\zeta)$ was reduced, until obtaining profiles which would seem unwise to the most adventurous of designers. Professor Peter Bradshaw (2004), in a personal communication to the author, opined that $f(\zeta)=0.5$ seems “just about right”, and the author is inclined to agree. Thus, the values of 0.613 and 0.387 were chosen for the first steps in the golden section search, with a termination criteria of a change less than 10^{-5} . The search terminated after only 3 iterations, returning 0.329 as the nearly optimal value for $f(\zeta)$. Indeed, calculated displacement thicknesses at the outlet differed very slightly from iteration to iteration, remaining about 1/20 of a millimeter. The change in construction necessary to implement the optimized shape over the closest, non optimal shape is well beyond the threshold of constructability. That being the case, the value of

$f(\zeta)=0.5$ has been chosen as it is both conservative, and close to the root 5th order polynomial already in service in so many tunnels (Bell & Mehta, 1988).

The function was further pushed until a vena contracta separation was observed at the outlet, occurring at $f(\zeta)=0.176$. Contour plots of the resultant velocity are shown in Figure 34.

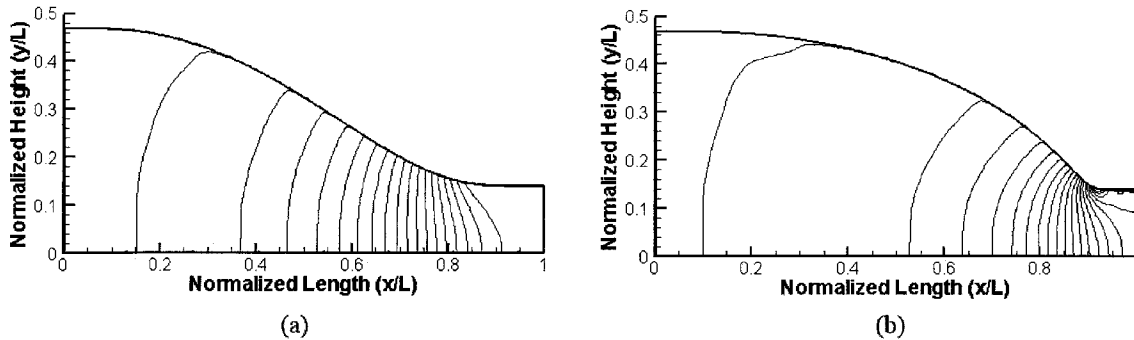


Figure 34: Normalized velocity contours for two contraction wall profiles, $f(\zeta)=0.5$ (a), and $f(\zeta)=0.137$ (b). Note the separation in the second case.

The construction method chosen was simple welded steel, as it could be done by a local contractor, given that an algebraically expressed function for the tunnel wall makes output of cutting templates for sheet metal trivial. 14 gauge steel was chosen, as the upstream pressure of an 86 m/s wind tunnel is considerable. The contraction as implemented is shown in Figure 35.



Figure 35: The contraction, as implemented.

4.8 Test Chamber

The design concept behind the test chamber was detailed in chapter 2.2, so all that remains is a discussion of the specific implementation. Considerable structural strength is required for the eventual implementation of the proposed vortex generator from Section 2.1. It was decided to take advantage of the strength and dimensional tolerance inherent in 6061-T6 aluminum extrusions (Figure 36).

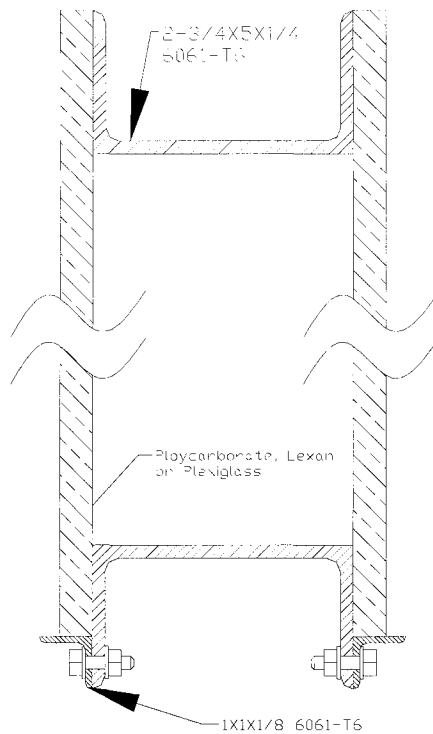


Figure 36: Cross section view of the 2D test section. Easily constructed from aluminum structural shapes, the fastening of the walls to the floor and ceiling is by clamping pressure.

The top and bottom walls are simply aluminum “C” channel of the appropriate width. Along the bottom wall, smaller 1x1x1/8 aluminum extrusions are bolted to provide a place for Lexan side walls to sit. Clamping pressure holds on the side walls, in the form of small woodworker’s hand clamps. It is common to see Lexan and Plexiglass crack at any small stress concentration, so it is hoped that the use of clamping pressure, which obviates the need for drilled holes, will prevent cracking. The test chamber is shown as implemented in Figure 37.



Figure 37: The test chamber, as implemented. Notice the slot milled in the bottom wall to permit the PIV laser to pass.

4.9 Diffusers

The unfortunate consequence of the 5 cornered square concept for the tunnel is that the inlet of the fan does not lie on the vertical plane through the center of the test section. Hence, it is necessary to divert the flow. It was chosen to try to achieve the ideal of a diffuser having tangential walls to the inlet, and at least partially at the outlet, and use this to divert the flow through the $\sim 4.5^\circ$ necessary, at this point.

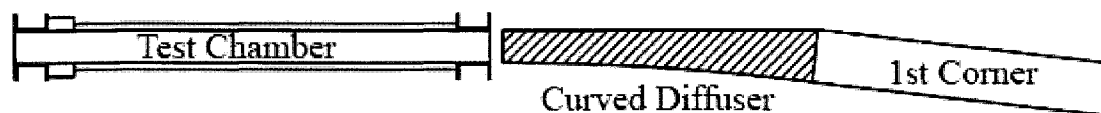


Figure 38: The present curved diffuser, shown hatched, between the test chamber (left) and the first corner (right).

Figure 38 shows the concept of the diffuser which incorporates a 4.5° turn. It has parallel top and bottom walls, and the side walls change from 5" to 8", dropping the velocity from 85 m/s to 53 m/s. At the inlet, both walls are tangent to the flow. The straight wall remains parallel to its associated test chamber wall, and meets the inlet to the first corner at 4.5° . The opposite wall follows a circular curve, and meets the inlet to the first corner at a tangent.

At the suggestion of Professor Paul Straznicky (2004), in a personal communication to the author, a vent is placed at the entrance to the diffuser, which drives this location to 0 gage pressure. As a consequence, every other part of the tunnel is at positive pressure with respect to the laboratory, thus, any leaks will be outward, and not energize boundary layers with inflow.

This curved and turning diffuser is only partly successful. Initial tests showed that there is separation occurring in it, to some extent, as the pressure drops just inside the inlet. This may be due to excessive amounts of air which must be re-entrained here, owing to prior leaks. However, by the end of the diffuser, sufficient pressure recovery has occurred to bring the pressure inside the tunnel higher than in the laboratory. This region may bear further investigation and/or remediation. Nevertheless, the tunnel performance is still acceptable. The diffuser following the test chamber is shown as implemented in Figure 39.

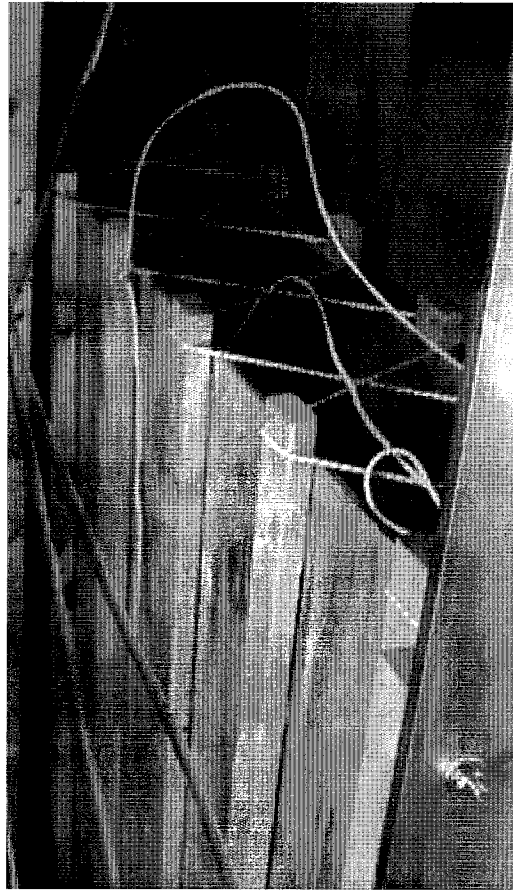


Figure 39: The diffuser immediately following the test chamber , as implemented.

4.10 Corner Vanes

The corner vanes were rolled (laboriously) by hand from 16 gauge galvanized steel sheet. A series of matching grooves were cut in sheets of $\frac{3}{4}$ " medium density fiberboard using a computer numerical controlled router. Indeed, the slots for the first two corners were inscribed on the same two sheets of fiberboard, and the first two corners built as a unit. This was a very simple way to implement corner vanes, in the opinion of the author. Unfortunately, there are no graphics to describe this process, however a schematic is show in Figure 40.

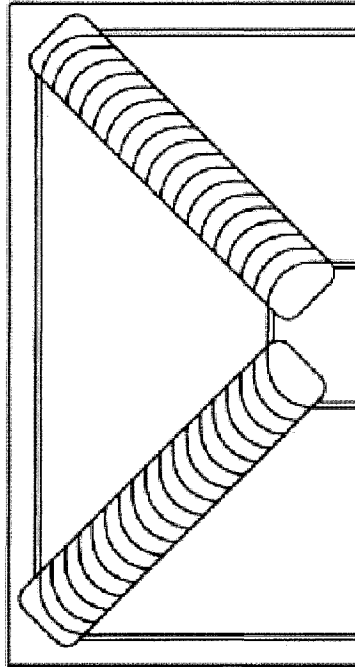


Figure 40: Schematic view of the corner vane slots inscribed in medium density fiberboard, to create the first two corners.

The assembly combining the first and second corners is shown as implemented in Figure 41.

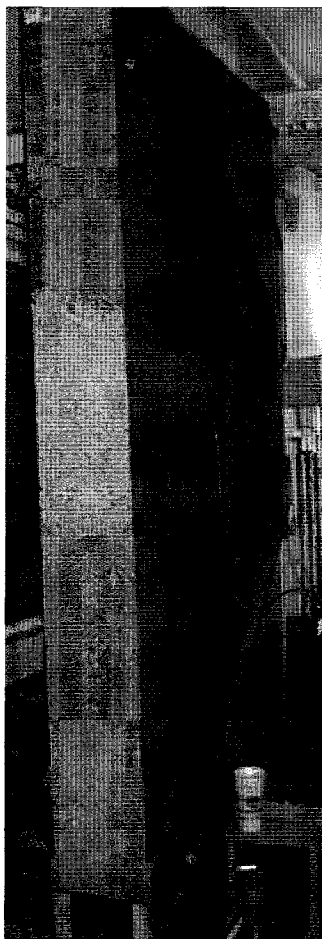


Figure 41: The first and second corner vanes in their assembly, as implemented.

4.11 The Blower

As discussed in Section 4.8, under certain circumstances, centrifugal blowers can be more suitable to duty in wind tunnels than axial fans. For the current tunnel, only off-the-shelf air handling units were considered which would not grossly overuse the limited space available. The New York Blower company, of Willowbrook, Illinois, produces a variety of quite suitable air handling units, as well as has selection software available. This software allows the designer to specify flow and pressure requirements and

generates an array of suitable products, complete with system, pressure, and mechanical input charts.

It is important to have some benchmark for a decision between a centrifugal blower and an axial fan. Taking the 17,000 ft³/min (8 m³/s) figure as a design requirement, two design philosophies are viable: 1) achieve, to the greatest extent, the lowest level of losses within the tunnel, which allows use of an axial fan, or 2) accept a much larger level of losses within the tunnel, simplifying design and construction, thereby greatly reducing cost in these areas while demanding a much greater level of pressure from the fan or blower. It became apparent during preliminary project evaluation that the precision manufacturing required for option 1 would be prohibitive. Using the design rules laid out in chapter 4, and assuming worst cases for losses (ie. simple construction), losses within the current tunnel were calculated at 7 inches of water.

Table 6: Summary of head losses in the current wind tunnel.

Location	Head Loss(m²/s²)
Wide Angle Diffuser	230
Settling Chamber	98
Test Section & Contraction	10
Sum of Corners	784
Return Path Ducting	335
total	1457

A conversion of the total head loss given in Table 6 to pressure, and then inches of water, the specification used by New York Blower, Inc, results in 7.05 inches of water. It is necessary to reduce head losses to 3 inches of water to select a suitable axial fan,

which would be quite a feat. Comparisons of these head loss figures with Figure 42 & Figure 43 demonstrate the advantage of the centrifugal blower in this application.

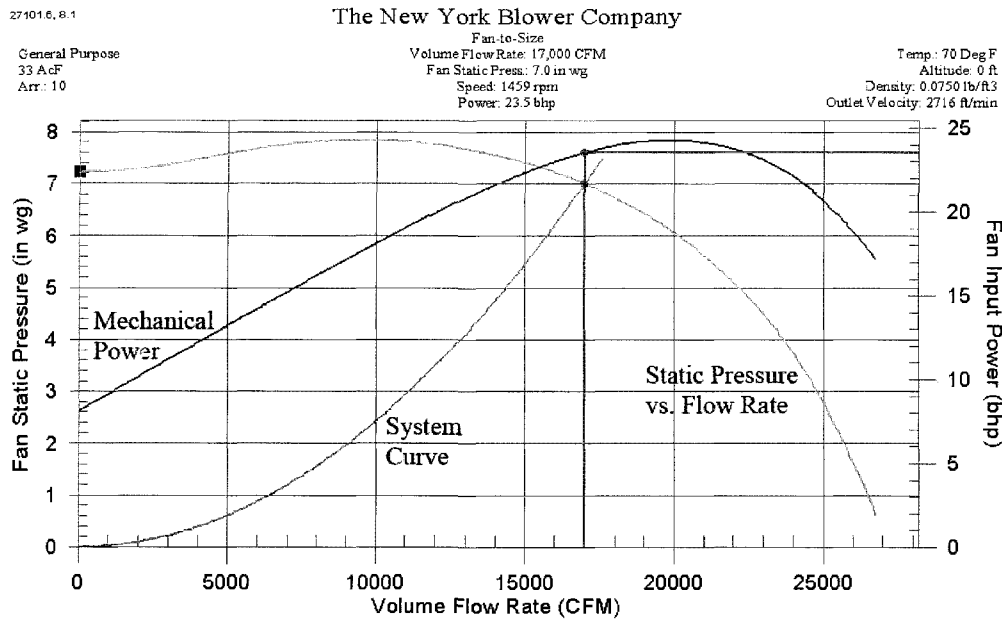


Figure 42: Performance curves for selected centrifugal blower.

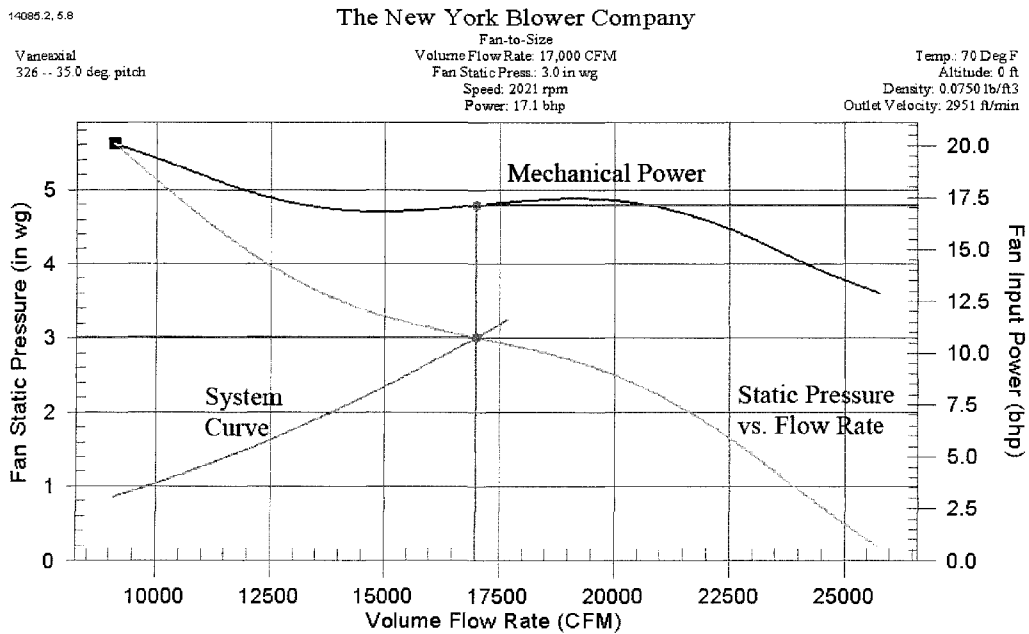


Figure 43: Performance curves for an axial fan, New York Blower model Vaneaxial 32".

The only motivation for use of an axial fan is to reduce power requirements. The head loss of 7 inches H₂O corresponds with a pressure drop of 1190 Pa. The head loss of 3 inches H₂O corresponds with a pressure drop of 509 Pa. The fan input power for the centrifugal blower (Figure 42) is 24 hp, or 17,897 Watts, while the fan input power for the axial fan (Figure 43) is 17.5 Hp, or 13050 Watts. The power output of an air handling unit, expressed in Watts is the flow rate in m³/s multiplied by the pressure change in Pa (N/m²). Thus the output power for the centrifugal and axial blowers are 9520 Watts and 4072 Watts respectively, giving efficiencies of 53% for the centrifugal blower, and 31% for the axial fan. In spite of the vast increase in cost and complexity associated with reducing losses in the tunnel to 3 inches H₂O, the fan efficiency falls so far in the selection of an axial fan that the input power savings is only 27% (24 Hp-17.5 Hp)/24 Hp.

The fan selected was the New York Blower company's General Purpose Acoustafoil 33 inches centrifugal blower.

4.12 Test Chamber Flow Testing

It would be ideal to evaluate the flow in the test chamber by taking a complete profile at the inlet, midpoint and outlet of the chamber, recording average velocity, turbulence intensity, and flow angularity using appropriate instrumentation. Unfortunately, time constraints and equipment unavailability made a rigorous commissioning of the current tunnel impossible.

As some measure of design success is nevertheless necessary, a pitot tube and vertical water manometer was used to generate profiles at the inlet and outlet of the tunnel, as shown in Figure 44:

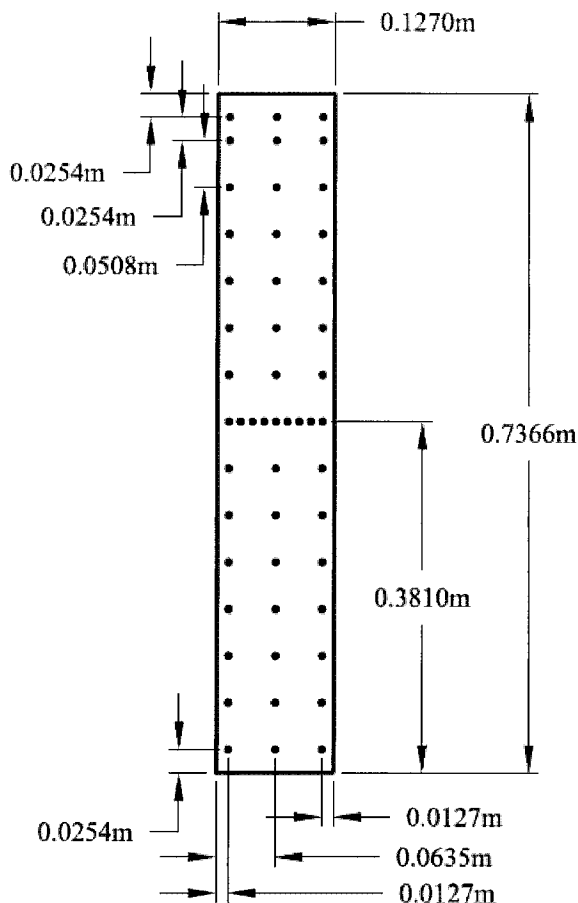


Figure 44: Grid of velocities recorded at inlet and outlet of test chamber.

The blower is equipped with a variable frequency drive , so the blower output is controlled by the frequency supplied to the AC motor. Readings were taken at 20Hz, 40Hz, and 60 Hz (maximum). Results of these readings appear in Table 7, and graphically summarized in Figure 45.

Table 7: Test Chamber velocities.

Inlet, Vertical, Left				Inlet, Vertical, Center				Inlet, Vertical, Right			
Position (m from bottom)	20 Hz V(m/s)	40 Hz V(m/s)	60 Hz V(m/s)	Position (m from bottom)	20 Hz V(m/s)	40 Hz V(m/s)	60 Hz V(m/s)	Position (m from bottom)	20 Hz V(m/s)	40 Hz V(m/s)	60 Hz V(m/s)
0.7112	22.0	50.2	78.3	0.7112	24.2	51.8	77.6	0.7112	20.5	51.3	76.0
0.6858	24.3	52.3	79.2	0.6858	24.7	52.4	78.6	0.6858	23.9	51.8	79.0
0.635	24.3	52.3	79.2	0.635	24.5	52.4	78.6	0.635	23.9	52.1	79.0
0.5842	24.5	52.3	78.7	0.5842	24.5	52.4	78.6	0.5842	23.9	52.1	79.0
0.5334	24.5	52.3	78.5	0.5334	24.5	52.4	78.3	0.5334	24.0	51.9	78.4
0.4826	24.5	52.3	77.9	0.4826	24.5	52.4	78.3	0.4826	24.0	51.7	78.4
0.4318	24.5	52.2	77.9	0.4318	24.5	52.4	78.1	0.4318	24.0	51.7	78.3
0.381	24.5	52.2	78.0	0.381	24.5	52.3	78.1	0.381	24.0	51.6	78.3
0.3302	24.5	52.3	78.0	0.3302	24.6	52.2	78.1	0.3302	24.0	51.6	78.1
0.2794	24.5	52.3	78.0	0.2794	24.6	52.2	78.2	0.2794	24.1	51.6	77.3
0.2286	24.5	52.5	78.3	0.2286	24.6	52.2	78.3	0.2286	24.2	51.6	77.3
0.1778	24.5	52.6	78.6	0.1778	24.6	52.3	78.4	0.1778	24.2	51.6	77.5
0.127	24.5	52.7	79.0	0.127	24.6	52.3	78.5	0.127	24.2	51.9	77.7
0.0762	24.5	52.9	79.3	0.0762	24.7	52.3	78.8	0.0762	24.2	51.9	78.1
0.0254	24.7	52.9	79.4	0.0254	24.7	52.6	78.7	0.0254	24.2	51.9	78.0

Outlet, Vertical, Left				Outlet, Vertical, Center				Outlet, Vertical, Right			
Position (m from bottom)	20 Hz V(m/s)	40 Hz V(m/s)	60 Hz V(m/s)	Position (m from bottom)	20 Hz V(m/s)	40 Hz V(m/s)	60 Hz V(m/s)	Position (m from bottom)	20 Hz V(m/s)	40 Hz V(m/s)	60 Hz V(m/s)
0.7112	21.7	44.5	64.4	0.7112	21.3	45.2	64.7	0.7112	21.2	45.6	68.3
0.6858	22.3	47.4	70.3	0.6858	25.2	54.7	82.6	0.6858	22.1	49.3	73.9
0.635	22.3	47.4	69.7	0.635	25.2	54.9	82.6	0.635	22.3	49.3	74.0
0.5842	22.3	47.6	69.7	0.5842	25.2	54.9	82.7	0.5842	22.3	49.6	72.5
0.5334	22.7	47.8	69.4	0.5334	25.2	55.1	82.7	0.5334	22.3	49.9	72.5
0.4826	22.7	47.7	67.7	0.4826	25.3	55.1	82.7	0.4826	22.3	50.0	73.8
0.4318	22.7	45.9	63.1	0.4318	25.3	55.1	82.8	0.4318	22.5	47.9	76.1
0.381	22.8	44.7	63.5	0.381	25.3	55.1	82.9	0.381	22.5	46.6	76.7
0.3302	23.1	44.9	64.1	0.3302	25.3	55.1	83.0	0.3302	23.0	47.0	76.7
0.2794	22.9	45.5	66.5	0.2794	25.3	55.2	83.2	0.2794	23.0	47.7	75.5
0.2286	22.6	46.7	68.6	0.2286	25.3	55.3	83.2	0.2286	23.0	48.9	75.1
0.1778	22.6	47.3	68.8	0.1778	25.6	55.3	83.2	0.1778	23.0	49.4	75.5
0.127	22.9	47.6	69.4	0.127	25.6	55.4	83.8	0.127	23.0	49.4	75.1
0.0762	23.1	48.1	70.8	0.0762	25.6	55.3	83.9	0.0762	23.0	49.9	76.1
0.0254	22.5	47.0	70.2	0.0254	24.5	53.3	81.1	0.0254	21.8	49.0	75.3

Inlet, Horizontal, Center				Outlet, Horizontal, Center			
Position (m from left)	20 Hz V(m/s)	40 Hz V(m/s)	60 Hz V(m/s)	Position (m from left)	20 Hz V(m/s)	40 Hz V(m/s)	60 Hz V(m/s)
0.0127	24.0	51.6	76.8	0.0127	23.7	46.7	77.1
0.0254	24.0	51.7	77.4	0.0254	25.3	53.7	82.0
0.0381	24.0	51.9	77.9	0.0381	25.3	55.1	82.9
0.0508	24.0	52.1	78.1	0.0508	25.4	55.1	83.0
0.0635	24.0	52.1	78.1	0.0635	25.4	54.9	83.2
0.0762	24.0	52.1	78.1	0.0762	25.3	54.9	83.5
0.0889	24.3	52.1	78.1	0.0889	25.1	54.7	83.1
0.1016	24.6	52.1	78.1	0.1016	25.0	54.1	78.2
0.1143	24.4	52.1	77.9	0.1143	23.6	51.5	66.7

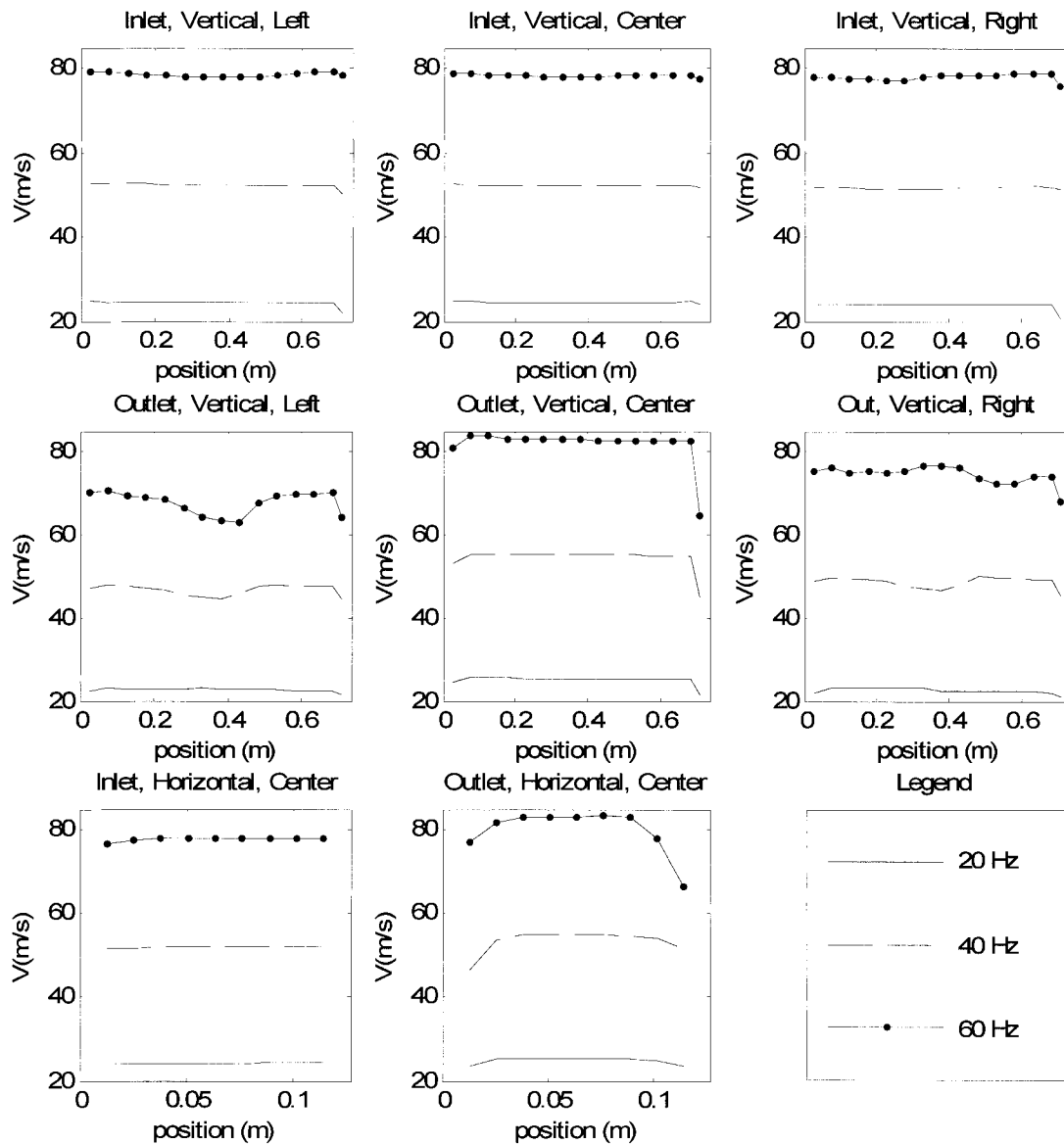


Figure 45: Velocity profiles in test chamber, associated with data from Table 7.

Examination of Figure 45 suggests that the tunnel implementation is successful. Unbounded flow is effectively represented through the center portion of the tunnel, from the inlet to the outlet. Centerline velocities are approximately 7% low. It is believed that this is the result of the only partial success of the first diffuser, which bends the flow

through 4.5° . Figure 46 & Figure 47, below show a rake manometer connected to various areas of the current wind tunnel.

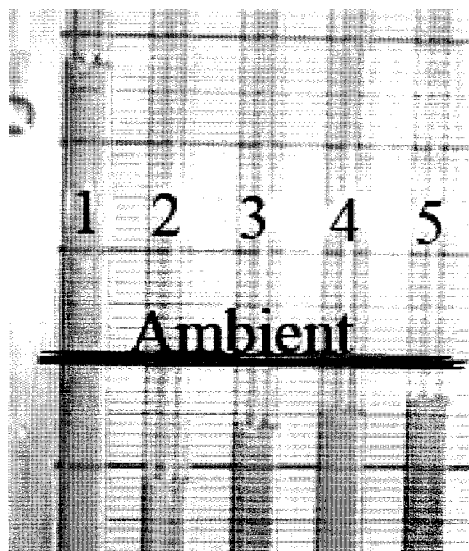


Figure 46: Detail of a rake manometer, connected to various points along the return path, as detailed in Figure 47.

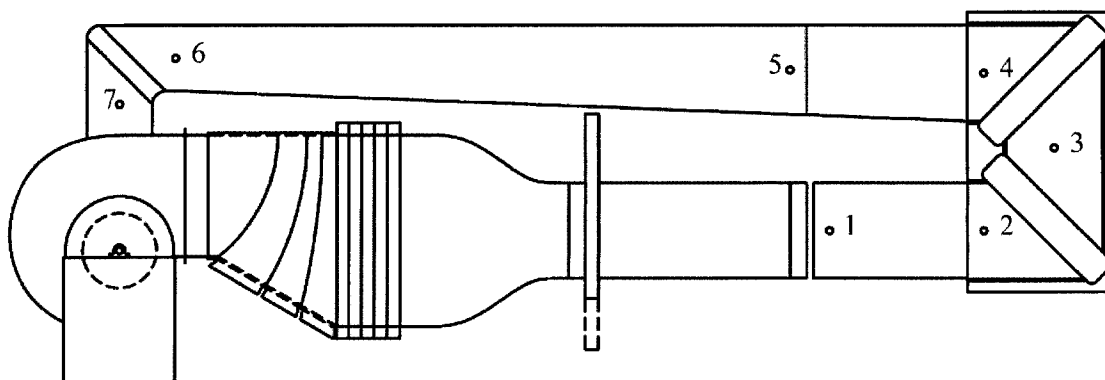


Figure 47: The connection points of the rake manometer.

Examination of Figure 46 and Figure 47 show that the pressure drop across the first set of corner vanes (2-3) is greater than that across the second set of vanes (3-4). This is likely due to re-circulation in the first diffuser causing flow angularity to stall

some of the corner vanes in the first corner. Turbulence introduced in that first set of vanes seems to permit the flow to traverse the second set of vanes much more smoothly. This points to the first diffuser as an area where some sort of remedial effort would be beneficial. It may be as simple as somehow introducing turbulence in this region, or reducing leaks upstream, thus air re-entrainment in the first diffuser region.

Given the extremely narrow space in which the current tunnel was implemented, it is difficult to obtain useful photographs of the facility. An airline diagram of the current tunnel appears in Figure 48.

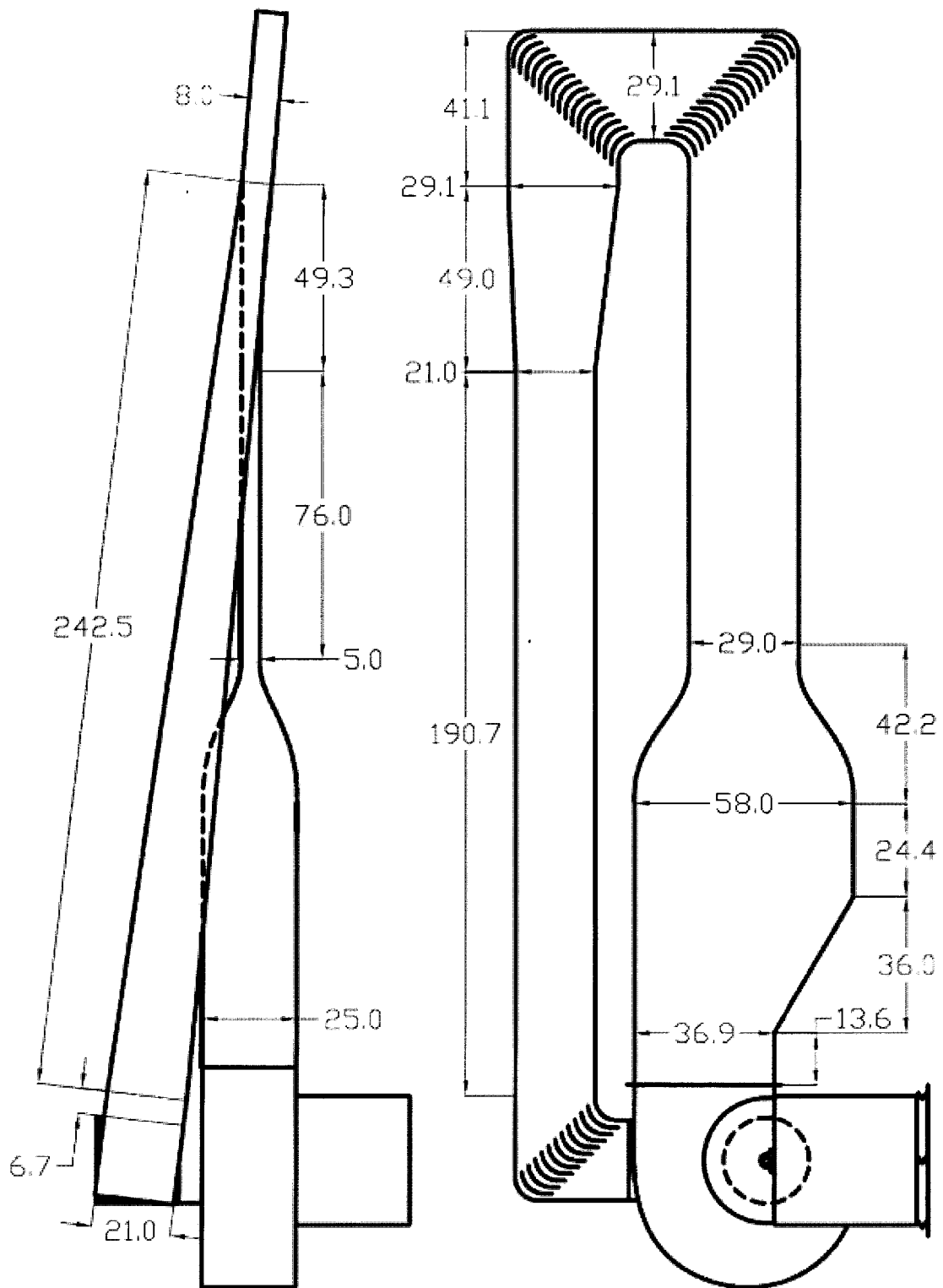


Figure 48: Airline diagram of the wind tunnel, all dimensions are in inches.

5. CONCLUSIONS AND RECOMMENDATIONS

A 2-D Transverse Vortex Wind Tunnel, designed to allow experiments in Airfoil-Vortex Interaction has been successfully implemented. It is capable of 80 m/s flow, and preliminary results suggest the flow uniformity is satisfactory.

The tunnel is ready for installation of the proposed vortex generator, though it is important to note that virtually any design of vortex generator is compatible with this design.

Detailed commissioning trials must be completed before this tunnel is ready to place in service, consisting of measurements of the flow angularity and turbulence intensities across the cross section, and along the length of the test chamber.

References

Lee, S., Bershader, D., "Head-On Parallel Blade Vortex Interaction", *AIAA Journal*, v 32, n 1, Jan, 1994, p 16-22

Yung H. Yu, "Rotor blade-vortex interaction noise", *Progress in Aerospace Sciences*, v 36, n 2, Feb, 2000, p 97-115

Morvant, R., Badcock, K.J., Barakos, G.N., Richards, B.E. "Study of blade/vortex interaction using computational fluid dynamics and computational aeroacoustics" *AHS International 4th Decennial Specialists' Conference on Aeromechanics*, 2004, p 641-670

Korber S., Ballman J., "Mechanisms and acoustics of Blade Vortex Interactions", *Z. J. Flugwiss. Weltraumforsch.*, vol.19, 1995, pp. 397-406

Yu Y.H., Gmelin B., Splettstoesser W., Phillipe J.J., Prieur J., Brooks T.F., "Reduction of helicopter blade vortex interaction noise by active rotor control technology", *Progress in Aerospace Science*, vol. 33, 1997, pp. 647-687

Splettstoesser, W.R., Junker, B., Schulthz, K.J., Wagner, W., Weitemeyer, W., Protopsaltis, A., Fertis, D., "The HELINOISE Aeroacoustic Rotor Test in the DNW, Test Documentation and Representative Results" *DLR (German Aerospace Center) DLR_Mittlung*, 1993,

Caradona, F. X., Strawn, R. C., Bridgeman, J. O., "An Experimental and Computational Study of Rotor-Vortex Interaction, *Vertica* 12, 1988

Strauss, J., Renzoni, P., Mayle, R. E., "Airfoil Pressure Measurements during a Blade Vortex Interaction and comparison with Theory", *American Institute for Aeronautics and Astronautics 26th Aerospace Science Meeting, Reno, Nevada*, 1988

Selerowicz, W., Siberaj, G., Szumowski, A., Piechna, J., "Effect of Miss-Distance on the Airfoil Vortex Interaction Experiment", *Arch, Mech*, 1998

Lent, H.-M., Meier, G.E.A., Mueller, K.J., Obermeier, F., Schievelbusch, U., Schuermann, O. "Mechanisms of transonic blade-vortex interaction noise", *Journal of Aircraft*, v 30, n 1, Jan-Feb, 1993, p 88-93

Mamou, M., Khalid, M., Xu, H., "Unsteady flows past two airfoils in tandem and airfoil-vortex interaction", *Canadian Aeronautics and Space Journal*, v 47, n 4, December, 2001, p 357-366

Lyn, D.A., Einav, S., Rodi, W., Park, J.-H., "Laser-Doppler velocimetry study of ensemble-averaged characteristics of the turbulent near wake of a square cylinder" *Journal of Fluid Mechanics*, v 304, Dec 10, 1995, p 285-319

Wilder M.C, Pesce M.M., Telonis D.P., Poling D.R., Dadone L., "Blade vortex interaction experiments – velocity and vorticity fields, 28th Aerospace Sciences Meeting conference paper, January 1990.

R.W. Fox, R.W., MacDonald, A.T., "Introduction to Fluid Mechanics" *John Wiley & Sons, Inc.* 1994

Davis, G.L., Feszty, D., Nitzsche, F., "Trailing edge flow control for the mitigation of dynamic stall effects", Paper 053, 31st European Rotorcraft Forum, Florence, Italy, 12-16 September 2005.

Mehta R.D., "Turbulent Boundary Layer Perturbed by a Screen", *AIAA Journal*, vol. 23, September 1985, pp. 1335-1342.

Bradshaw, P., and Mehta R.D., "Wind Tunnel Design", *website*
<http://vonkarman.stanford.edu/tsd/pbstuff/tunnel/index.html>, 2003

Mehta R.D & Bradshaw P., "Design rules for small, low speed wind tunnels", *Aeronautical Journal of the Royal Aeronautical Society*, vol. 1, November 1979, pp. 443-449.

Weighart K.E., "On the resistance of screens", *Aero Quarterly*, Vol 4, 1953. pp. 186

Bell J.H. & Mehta R.D., "Contraction Design for Small, Low Speed Wind Tunnels", *NASA contractor report*, 1988

Bradshaw, P. personal communication, 2004.

Brassard D.P., Ferchichi M., "Transformation of a Polynomial for a Contraction Wall Profile", *Journal of Fluids Engineering, Transactions of the ASME*, v 127, n 1, January, 2005, p 183-185

Straznicky, P., personal communication, 2004.

Lindgren, B., Johansson, A.V., "Evaluation of a New Wind Tunnel With Expanding Corners" *Experiments in Fluids*, Vol. 36, 2004, pp. 197-203.

Sahlin, Se., A.V. Johansson, A.V., "Design of guide vanes for minimizing the pressure loss in sharp bends", *Phys. Fluids A3*, 1934, 1991